

RL-TR-94-142
Final Technical Report
August 1994

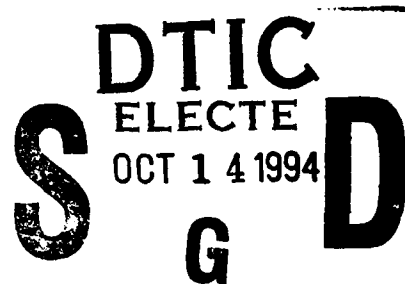


DESIGN AND FABRICATION OF NxN OPTICAL COUPLERS BASED ON ORGANIC POLYMER OPTICAL WAVEGUIDES

Washington University

Robert R. Krchnavek and Daniel L. Rode

AD-A285 530



APPROVED FOR PUBLIC RELEASE; DISTRIBUTION UNLIMITED.

DTIC QUALITY INSPECTED 2

**Rome Laboratory
Air Force Materiel Command
Griffiss Air Force Base, New York**

448

94-32194



9410 03 7

This report has been reviewed by the Rome Laboratory Public Affairs Office (PA) and is releasable to the National Technical Information Service (NTIS). At NTIS it will be releasable to the general public, including foreign nations.

RL-TR-94-142 has been reviewed and is approved for publication.

APPROVED:



RAYMOND K. BONCEK
Project Engineer

FOR THE COMMANDER:



LUKE L. LUCAS, Colonel, USAF
Deputy Director of Surveillance & Photonics

If your address has changed or if you wish to be removed from the Rome Laboratory mailing list, or if the addressee is no longer employed by your organization, please notify RL (OCPA) Griffiss AFB NY 13441. This will assist us in maintaining a current mailing list.

Do not return copies of this report unless contractual obligations or notices on a specific document require that it be returned.

REPORT DOCUMENTATION PAGE

Form Approved
OMB No. 0704-0188

Public reporting burden for this collection of information is estimated to average 1 hour per response, including the time for reviewing instructions, searching existing data sources, gathering and maintaining the data needed, and completing and reviewing the collection of information. Send comments regarding this burden estimate or any other aspect of this collection of information, including suggestions for reducing this burden, to Washington Headquarters Services, Directorate for Information Operations and Reports, 1215 Jefferson Davis Highway, Suite 1204, Arlington, VA 22202-4302, and to the Office of Management and Budget, Paperwork Reduction Project (0704-0188), Washington, DC 20503.

1. AGENCY USE ONLY (Leave Blank)		2. REPORT DATE August 1994		3. REPORT TYPE AND DATES COVERED Final Jan 93 - Jan 94	
4. TITLE AND SUBTITLE DESIGN AND FABRICATION OF NxN OPTICAL COUPLERS BASED ON ORGANIC POLYMER OPTICAL WAVEGUIDES				5. FUNDING NUMBERS C - F30602-93-C-0004 PE - 62702F PR - 4600 TA - P1 WU - PI	
6. AUTHOR(S) Robert R. Krchnavek and Daniel L Rode				8. PERFORMING ORGANIZATION REPORT NUMBER	
7. PERFORMING ORGANIZATION NAME(S) AND ADDRESS(ES) Washington University Campus Box 1054 One Brookings Drive St. Louis MO 63130-4899				10. SPONSORING/MONITORING AGENCY REPORT NUMBER RL-TR-94-142	
9. SPONSORING/MONITORING AGENCY NAME(S) AND ADDRESS(ES) Rome Laboratory/OCPA 25 Electronic Pky Griffiss AFB NY 13441-4515					
11. SUPPLEMENTARY NOTES Rome Laboratory Project Engineer: Raymond K. Boncek/OCPA/(315) 330-2937					
12a. DISTRIBUTION/AVAILABILITY STATEMENT Approved for public release; distribution unlimited.				12b. DISTRIBUTION CODE	
13. ABSTRACT (Maximum 200 words) In this report, we examine the design and fabrication of a planar, 10x10 optical coupler utilizing photopolymerizable organic polymers. Background information on the theory of operation of the coupler culminating in a set of design equations is presented. The details of the material processing are described, including the preparation of monomer mixtures that result in single-mode polymer waveguides ($\lambda = 1300$ nm) that have core dimensions approximately equal to those of single-mode fiber. This is necessary to insure high coupling efficiency between the planar device and optical fiber. A unique method of aligning and attaching optical fibers to the coupler is demonstrated. This method relies on patterned alignment ways, a transcision cut, and single-mode D-fiber. A theoretical analysis of the in situ monitoring technique used to fabricate the single-mode D-fiber is presented and compares favorably with the experimental results. Finally, the 10x10 coupler is characterized. We have measured an excess loss of approximately 8 dB. Several possible sources of loss are discussed.					
14. SUBJECT TERMS Optical waveguides, Polymers, Couplers, D-fiber				15. NUMBER OF PAGES 60	
				16. PRICE CODE	
17. SECURITY CLASSIFICATION OF REPORT UNCLASSIFIED	18. SECURITY CLASSIFICATION OF THIS PAGE UNCLASSIFIED	19. SECURITY CLASSIFICATION OF ABSTRACT UNCLASSIFIED	20. LIMITATION OF ABSTRACT UNLIMITED		

Table of Contents

Table of Contents	i
List of Figures	ii
Part I – Interim Report	1/2
Introduction	3
Design and Fabrication of an $N \times N$ Star Coupler	3
Coupler Geometry	4
Coupler Operation	5
Fourier Optics	5
Diffraction Through an Aperture	7
Development of Design Equations	11
Fabrication of Photomask	16
Refractive Index Measurement and Tailoring	18
Introduction	18
Fabrication of Monomer Blends	18
Refractive Index Measurement	19
D-fiber Fabrication and Testing	23
Conclusion	24
Part II – Final Report	25/26
Single-Mode D-Fiber	27
Theoretical Analysis	28
Experimental Results	31
Conclusion	40
Procedure for Making a Planar Star Coupler	41
Introduction	41
Preparation of Monomer Mixtures	41
Index Tailoring	42
Building the Coupler	43
Post-Cure Sample Preparation	45
Final Packaging	46
Loss Measurements on the $N \times N$ Star Coupler	47
Conclusion	49
Attachment – Reprints/Preprints of Published Work	50

Accession For	
NTIS	<input checked="" type="checkbox"/> CRA&I
DTIC	<input checked="" type="checkbox"/> TAB
Unannounced	<input type="checkbox"/>
Justification	
By	
Distribution /	
Availability Codes	
Dist	Avail and / or Special
A-1	

List of Figures

Part I – Interim Report

Figure 1.	Schematic plan view of a star coupler	5
Figure 2.	Artistic conception of coupler operation	6
Figure 3.	Waveform transients	6
Figure 4.	The Huygens-Fresnel principle	8
Figure 5.	Geometry for diffraction calculations	9
Figure 6.	Coupler geometry	11
Figure 7.	The ideal shape of the electric field	12
Figure 8.	The necessary shape of the electric field	13
Figure 9.	Assumed electric field	14
Figure 10.	Resulting shape of electric field	14
Figure 11.	Schematic plan view of a star coupler	15
Figure 12.	Diagram of alignment structures	17
Figure 13.	Polymer well structure and photomask pattern	19
Figure 14.	A Michelson interferometer	20
Figure 15.	An example of interference fringes	21
Figure 16.	Typical interferogram	21
Figure 17.	Graph of refractive index	22

Part II – Final Report

Figure 1.	Schematic diagram of an optical fiber	29
Figure 2.	Ray-tracing diagram	30
Figure 3.	Michelson interferogram	34
Figure 4.	Schematic diagram of the <i>in situ</i> monitoring setup	35
Figure 5.	Typical throughput attenuation versus lapping time	36
Figure 6.	Histogram and normal probability plot of throughput attenuation	38
Figure 7.	Histogram and normal probability plot of lapped depths	39
Figure 8.	Photomicrograph of a cross-section of a single-mode D-fiber	40

Part I – Interim Report

Introduction

Integrated optical devices are increasingly in demand for use as components in high-speed data networks. A particularly valuable component is the $N \times N$ optical coupler or star coupler. Although early methods of fabricating $N \times N$ couplers^{1,2} have been characterized by a high degree of optical loss due to poor internal coupling efficiency, recent work indicates that highly efficient star couplers can be fabricated based on Fourier optics and Rotman lens theory.

The proposed goal of this work is to design, fabricate and test a 10×10 single-mode star coupler using photo-patternable acrylic polymers. The use of these materials was based on several expected advantages: low optical loss at standard operating wavelengths, simple and low-cost processing over large areas, compatibility with materials and processing conditions involved in the fabrication of many optical devices, and high potential for tailoring of index of refraction necessary for single-mode operation.

Achieving efficient coupling between optical devices is a major problem in experimental optical systems, especially for those which utilize integrated optical devices such as the star coupler. In order to facilitate the coupling of single-mode fiber to the integrated optical waveguides of the star coupler, a novel method was also proposed to make use of D-fiber and polymer alignment structures.

Here, specifically is what was included in the proposal's Statement of Work:

- theoretical analysis of Fourier-optic designed $N \times N$ coupler leading to a set of design equations.
- design of photomask sets for a 10×10 coupler.
- modification of current polymer resins to examine their suitability for single-mode waveguides.
- fabrication of 10×10 couplers using the modified resins.
- measurement of the optical performance of the couplers.
- fabrication of D-fiber for novel fiber/waveguide coupling scheme.
- evaluation of the optical properties of D-fiber.
- mounting of D-fiber pigtails onto the 10×10 coupler.
- delivery of an interim progress report 6 months into the contract.
- delivery of a fiber coupled 10×10 coupler.
- delivery of a final progress report.

In this midterm report we present our progress to date, which concerns the first three subjects presented above in the Statement of Work as well as a brief description of our work on D-fiber fabrication. The first section, therefore, contains a discussion of star coupler theory and design and presents the specific design chosen for photomask fabrication. The second section presents our

¹ A. A. M Saleh and H. Kogelnik, J. Lightwave Technol. 6, 392 (1988)

² K. Iizuka, Engineering Optics, 2nd ed. (Springer-Verlag, New York, 1986), pp. 336-370.

work in modifying and measuring the index of refraction of our polymers. Finally, the third section is a summary of our work in fabricating D-fiber with reference to work we presented at the Electronic Components & Technology Conference (ECTC) early this summer.

Design and Fabrication of an $N \times N$ Star Coupler

Coupler Geometry

The type of star coupler which will be described in the following pages is unique, with respect to standard star couplers which we have seen in past literature, in that it is *planar*. In other words, each of its input and output optical pathways are located in the same plane. The ultimate use of this device in an optical system will be accomplished in this way: a number of optical fibers (the number depends on the number of inputs and outputs the device has been designed for) carrying the input and output signals will be mounted onto a chip, connecting to the input and output waveguides of the star coupler constructed on that chip. Alternately, the planar star coupler could be integrated into a board-level, integrated, optical system. This would preclude the use of optical fiber. Diagrammed in Fig. 1 is a general schematic (plan view) of the star coupler structure.

As can be seen, the coupler consists of an input and output array of waveguides which converge towards a central region. Each array terminates on an arc of a circle, indicated by the u and w axes. Each of the two circles passes through the center of the other, causing each waveguide in the input array to be directed towards the center of the output array, and vice versa. This geometry is analogous to that of a Rotman lens, used to create multiple beams in microwave antenna arrays.³

The central region is constructed of the same material as the waveguides. During single-mode operation, light is guided down a waveguide and enters into the central region, which acts like a slab waveguide and is sometimes referred to as the "free-space" region. However, there is no change in refractive index from the waveguide to the central region beyond that of a change from the effective index of the waveguide to the effective index of the slab region. The effect of light passing from the single-mode waveguide to the free-space region is analogous to light passing through an aperture. Given the small dimensions of a single-mode waveguide (width $< 10\mu\text{m}$), the light will be strongly diffracted. This effect is extremely important to the operation of this coupler, since it characterizes the spatial distribution of intensity which is seen by the receiving array. We will show that if the receiving array is in the far-field of the input array, then the intensity distribution at the receiving array $\psi(w)$ is related to that of the input array $\psi(u)$ by a spatial Fourier transform.

³ W. Rotman and R. F. Turner, IEEE Trans. Ant. Prop. 11, 623 (1963).

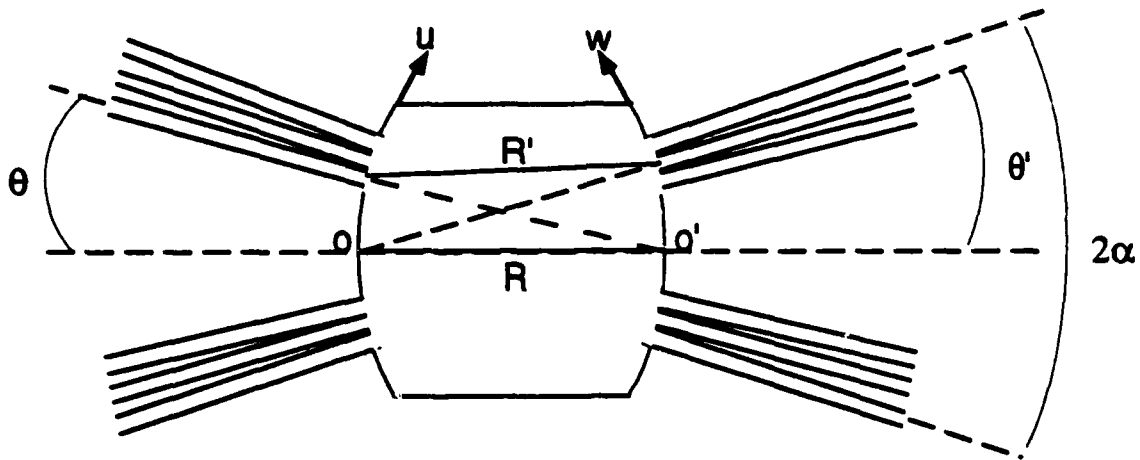


Figure 1. Schematic plan view of a star coupler, consisting of a planar arrangement of two linear arrays of waveguides which converge upon a central region. O and O' represent the center of the input and output arrays on the u and w axes respectively, while R is the distance between the two. R' labels the distance between an input and an output aperture located at an angle of θ and θ' respectively. Not detailed in this diagram are the structures at the ends of the waveguides which allow coupling to optical fiber.

Coupler Operation

The function of an $N \times N$ star coupler is to divide the power of each of N inputs evenly over N outputs. Fig. 2 is an artistic representation of coupler operation, where light is being input to a single waveguide. The beam spreads through the free-space region due to diffraction and illuminates the receiving array uniformly. The choice of the center waveguide is arbitrary and, if the coupler is designed efficiently, irrelevant. That is to say, regardless of which input waveguide is used the power will still be approximately evenly split among the output waveguides. Fig. 3 provides another perspective from which to view coupler operation.

Shown are a series of waveform transients calculated using the beam propagation method (BPM) by K. Okamoto *et al.*, for an 8×8 star coupler (ref. Okamoto). In the foreground (labeled "Input Array") the power distribution is that of light propagating in one single-mode waveguide. As the light propagates in the slab region, the power distribution changes shape, spreading and becoming flatter. Finally we see light coupling from the slab region to the output array, producing a nearly even split of optical power among the eight output waveguides.

Fourier Optics

The importance of Fourier optics for our work is that it provides a way of looking at the diffraction of light in the context of Fourier transforms. Describing optical diffraction in three or even just two dimensions may still require complicated mathematics, whereas a Fourier transformation is well understood and perhaps has even been worked out in advance in some text. The use of Fourier

transforms in describing the far-field distribution of light diffracted by an aperture leads to an easier understanding of coupler operation.

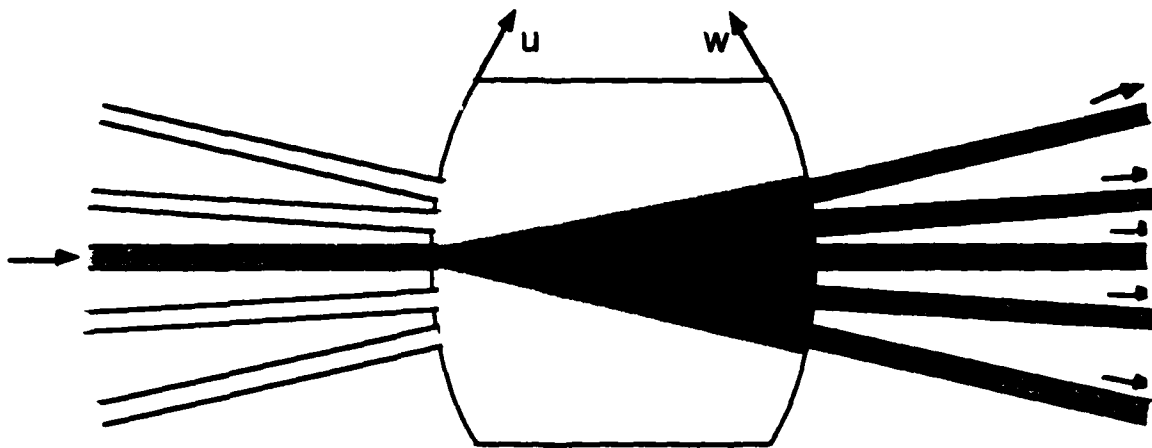


Figure 2. Artistic conception of coupler operation. Light input to a single waveguide spreads by diffraction in the free-space region and evenly illuminates the entire receiving array.

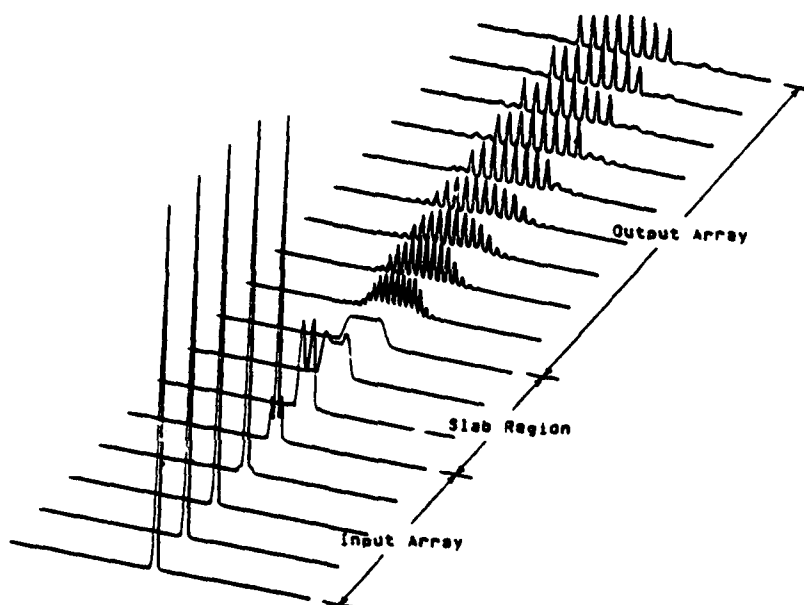


Figure 3. Waveform transients calculated by K. Okamoto *et al.* with the beam propagation method, showing the change in shape of the optical power distribution as light passes from a single waveguide, through the slab region, and into eight output waveguides.

A brief review of the concepts of Fourier series and transforms is appropriate here. A periodic signal $x_p(t)$ represented as the sum of weighted complex exponentials

$$x_p(t) = \sum_{-\infty}^{+\infty} a_n e^{jn\omega_0 t} \quad (1)$$

is called a Fourier series, where the weights

$$a_n = \frac{1}{T_0} \int_{T_0} x_p(t) e^{-jn\omega_0 t} dt \quad (2)$$

are the Fourier coefficients, T_0 is the period, and $\omega = n\omega_0$. Realizing that an aperiodic signal $x_a(t)$ can be thought of as a periodic signal ($x_a(t)$ repeated every T_0 seconds) with an infinite period, we see that an aperiodic signal can be represented by a continuum of weighted complex exponentials,

$$x_a(t) = \frac{1}{2\pi} \int_{-\infty}^{+\infty} X(\omega) e^{j\omega t} d\omega \quad (3)$$

where

$$X(\omega) = \int_{-\infty}^{+\infty} x_a(t) e^{-j\omega t} dt \quad (4)$$

is the Fourier transform of $x_a(t)$.

The next section will tie in the connection between the Fourier transform and the operation of the star coupler. It is important to realize that the coupler operation has nothing to do with a transformation from the time domain to the frequency domain. That is because with respect to the coupler we are talking about *spatial* Fourier transforms. What concerns us is a transformation from coordinates on the u axis to coordinates on the w axis (see Fig. 1) and the change in shape of the optical intensity distribution.

Diffraction Through an Aperture

The change in distribution of optical power that occurs from input array to output array is due to diffraction of the input signal as it enters the free-space region. Therefore let us now look at diffraction through an aperture in two dimensions. To begin let us consider a hypothetical image that may help clarify the effect of an aperture. The Huygens-Fresnel principle states that every unobstructed point of a wavefront at a given instant in time serves as a source of spherical secondary wavelets. In addition, the superposition of these wavelets gives the amplitude of the optical field at points beyond the wavefront. Fig. 4 shows the application of this principle to an aperture in an opaque screen. On the left of the figure is a wavefront in free-space. The wavelets from each secondary source superimpose to form the next identical wavefront. However, on the right the wavefront is partially obstructed. The field formed by the superposition of the unobstructed wavelets is much different than that existing before the aperture.

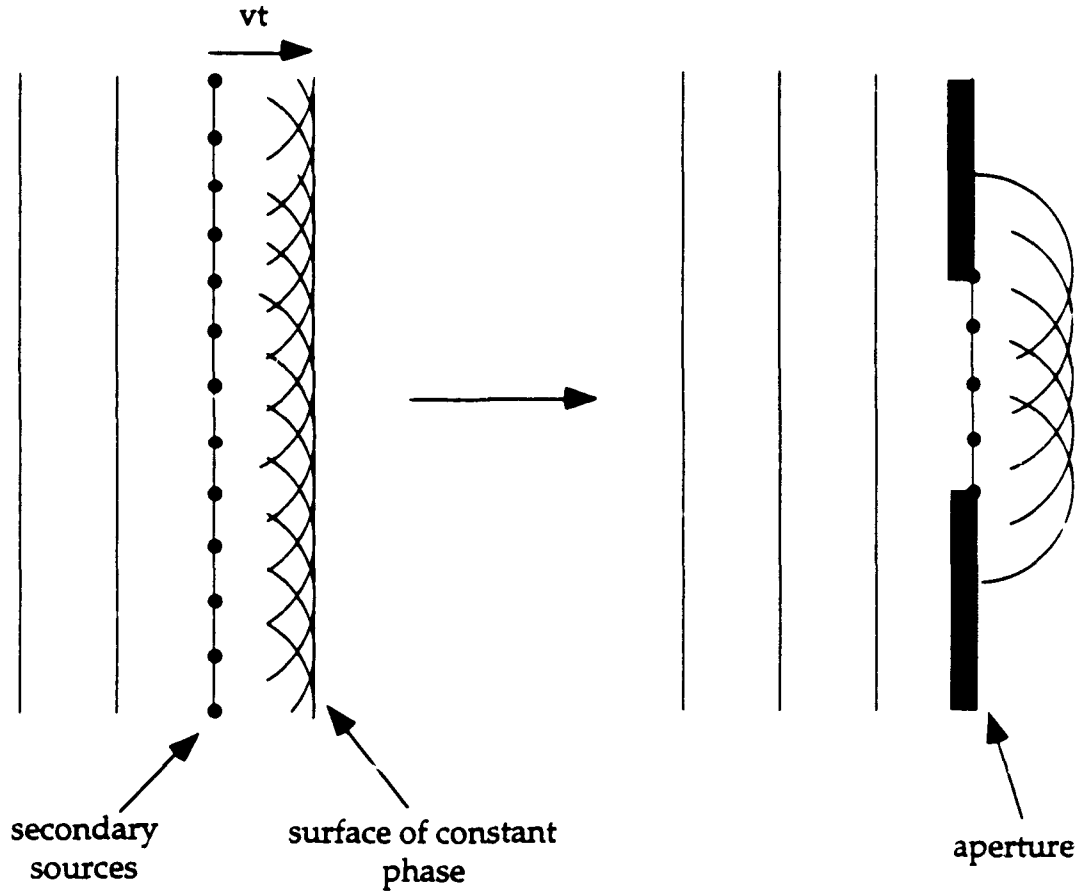


Figure 4. The Huygens-Fresnel principle. On the left is a wavefront in free-space, and on the right a wavefront influenced by an aperture in an opaque screen. Only the unobstructed portion of a wavefront may contribute to the next wavefront.

Now let us consider diffraction mathematically. The geometry we will use is presented in Fig. 5. We would like to determine the field at point P due to an arbitrary field existing at the input aperture. Later in this derivation we will convert from this basic geometry to that of our coupler. Let us imagine that the field at the input aperture consists of a series of point sources producing cylindrical waves, each having a strength $E_0(x)$ which is dependent on its position x . Then the field contributed by the i th point source is

$$E_i = \frac{E_0(x)}{\sqrt{R_i}} e^{jkR_i} \quad (5)$$

where R_i is the distance from the i th source to point P, and we have used the relation for a cylindrical wave.

If we allow the number of sources in the aperture to be large and therefore the distance between them infinitesimal, then we can represent the total field at P as

$$E(P) = \int_{-\frac{a}{2}}^{\frac{a}{2}} \frac{E_0(x)}{\sqrt{R(x)}} e^{jkR(x)} dx \quad (6)$$

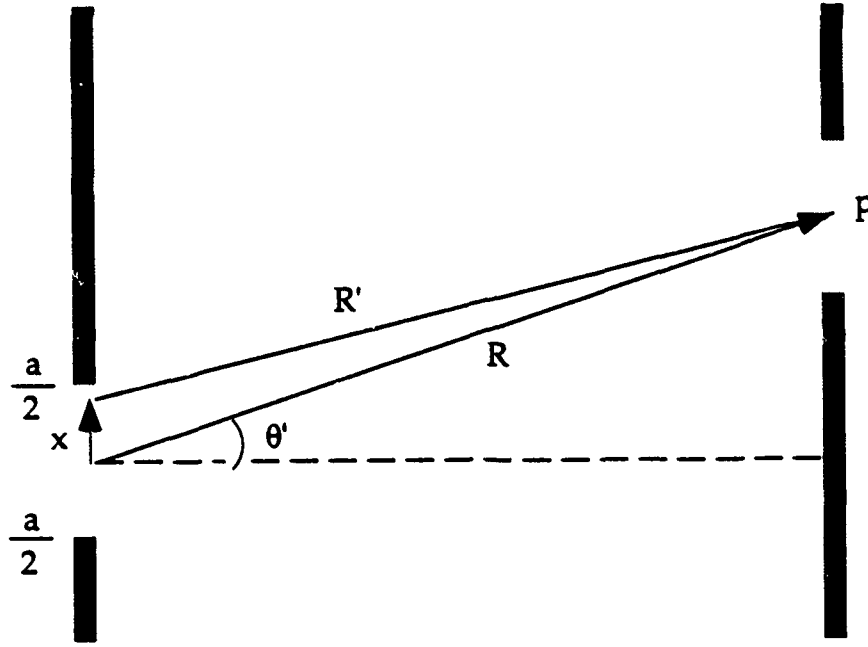


Fig. 5. Geometry for diffraction calculations. Point P at the output aperture is where we want to determine the field due to some field at the input aperture.

We may define $R(x)$ further using the law of cosines and referring to Fig. 5

$$R(x)^2 = R^2 + x^2 - 2xR\sin\Theta$$

and thus, using the first three terms of the binomial series,

$$R(x) = R \sqrt{1 + \frac{x^2 - 2xR\sin\Theta}{R^2}}$$

$$\approx R \left(1 - \frac{x\sin\Theta}{R} + \frac{x^2}{2R} \cos^2\Theta + O(x^3) \right)$$

so that we have

$$R(x) = R - x\sin\Theta + \frac{x^2}{2} \cos^2\Theta + O(x^3) \quad (7)$$

We now assume that the point P is very distant from the input aperture and that R is much, much greater than the aperture size. This is the same as saying that the point P is in the far-field of the input. We may now apply the Fraunhofer approximation to $R(x)$ in (6). The phase term is more sensitive to variations in $R(x)$ so it is treated differently from the denominator. In the phase term of (6) let

$$R(x) \approx R - x \sin \Theta'$$

and in the denominator of (6) let

$$R(x) \approx R$$

Therefore we have for the total field at point P

$$E(P) = \int_{-\frac{a}{2}}^{\frac{a}{2}} \frac{E_0(x)}{\sqrt{R}} e^{jk(R - x \sin \Theta')} dx$$

or

$$E(P) = \frac{e^{jkR}}{\sqrt{R}} \int_{-\frac{a}{2}}^{\frac{a}{2}} E_0(x) e^{-jkx \sin \Theta'} dx \quad (8)$$

Now that we have found an expression for the total field at point P for the basic geometry of Fig. 5, let us adjust this result to fit the geometry of our coupler, presented again in Fig. 6 for convenience.

In Fig. 6, from basic geometric principles we have

$$\begin{aligned} R' &= R \sqrt{(\sin \Theta - \sin \Theta')^2 + (\cos \Theta + \cos \Theta' - 1)} \\ &= R \sqrt{3 - 2 \sin \Theta \sin \Theta' + 2 \cos \Theta \cos \Theta' - 2 \cos \Theta - 2 \cos \Theta'} \end{aligned} \quad (9)$$

Here we will take advantage of foreknowledge of the dimensions of our coupler to apply a paraxial approximation. The entire angular extent 2α (see Fig. 1) of either the input or output arrays will encompass less than 1° . Therefore we may assume that

$$\cos \Theta = \cos \Theta' \approx 1 \quad (10)$$

Substituting (10) into (9) and expanding the square root in the first two terms of the binomial series we have

$$R' \approx R(1 - \sin \Theta \sin \Theta') \quad (11)$$

Finally, to find an expression for the electric field at point P', we can substitute (11) in for $R(x)$ in the phase factor of (6) and use $R(x) \approx R$ again in the denominator. Thus,

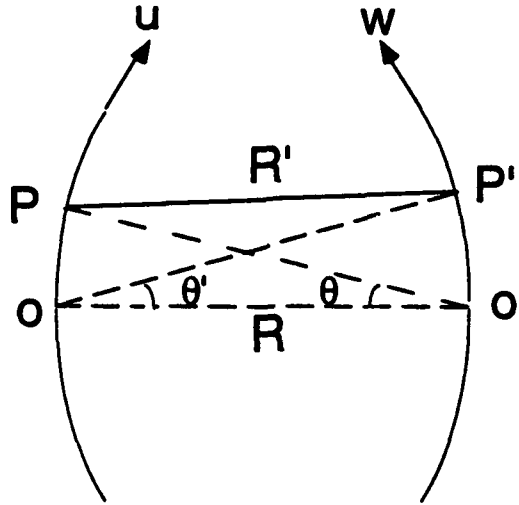


Fig. 6. Coupler geometry showing two apertures from the input and output arrays, located at points P and P' respectively. We want to calculate the field at point P' given an input at point P.

$$E(P') = \frac{e^{jkR}}{\sqrt{R}} \int_A E_0(x) e^{-jksin\Theta sin\Theta'} dx \quad (12)$$

where A represents the limits of the aperture at P, or

$$E(P') = \frac{e^{jkR}}{\sqrt{R}} F(\Theta, \Theta')$$

where

$$F(\Theta, \Theta') = \int_A E_0(x) e^{-jksin\Theta sin\Theta'} dx$$

One can see the similarity between the term $F(\theta, \theta')$ and the Fourier transform $X(\omega)$ in (4). In fact, with careful consideration of the variables involved and the duality of the Fourier and inverse Fourier transforms, one can treat $F(\theta, \theta')$ and $E_0(x)$ mathematically as a Fourier transform pair. The advantage gained here is obvious. Given any intensity distribution at the input to the free-space region of our coupler, actual or desired, we can calculate the field that the receiving array will see using Fourier transform mathematics.

Development of Design Equations

The development of design equations for the star coupler involved extensive use of a paper by C. Dragone entitled "Efficient $N \times N$ Star Couplers Using Fourier Optics" which appeared in the

Journal of Lightwave Technology, volume 7, number 3, March 1989. The following section will present a discussion of the development of the design equations.

Let us rewrite (12) using the notation found in Dragone's work. The input distribution $E_0(x)$ is now represented by $\psi(u)$, with $u = \sqrt{f(2a, x)}$ where a is the width of the aperture. Letting $x = R \sin \theta$ and performing a change of variable, (12) becomes

$$E(u, w) = \frac{e^{jkR}}{\sqrt{R}} \Phi(w) \quad (13)$$

where

$$\Phi(w) = \frac{1}{2} \int_{-1}^1 \Psi(u) e^{jw} du \quad (14)$$

and

$$w = \frac{\pi a \sin \Theta'}{\lambda} \quad (15)$$

We can see by reviewing the coupler geometry shown in Fig. 1 that the waveguides of the receiving array are side-by-side at the boundary of the free-space region. Ideally, if the light from the input aperture were to evenly illuminate the receiving array, that would represent the most efficient configuration. In other words, the electric field distribution at the output array should be a rectangular function

$$\Phi(w) = A \text{ rect} \left(\frac{2w}{w_\alpha} \right)$$

such as shown in Fig. 7.

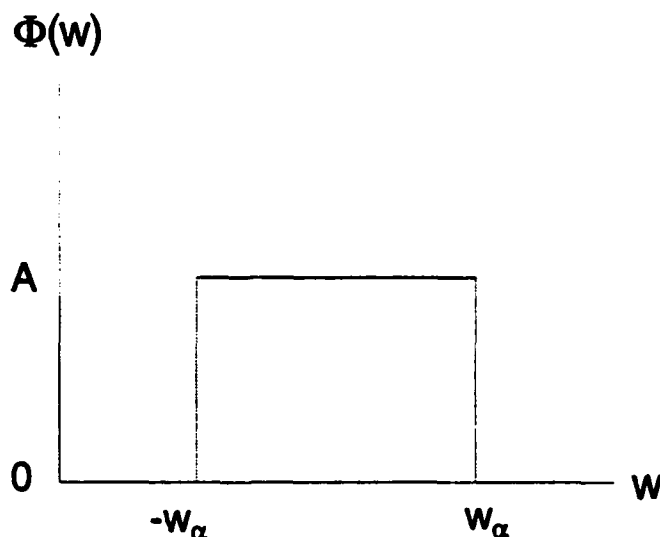


Figure 7. The ideal shape of the electric field distribution at the output is a rectangular function with a width that spans the entire angular extent of the output array.

Recall from (15) that w is a normalized variable representing position on the w axis. In Fig. 7 and in the following figures w_α is simply w , as represented (15), with $\theta' = \alpha$

$$w_\alpha = \frac{\pi a \sin \alpha}{\lambda}$$

The values w_α and $-w_\alpha$ represent the positions of the outermost waveguides of the receiving array on w . However, we need only take the Fourier transform of the rectangular function shown in Fig. 7 to determine the shape of the distribution needed at the input to produce such a distribution at the output. Not surprisingly, we see that we would need

$$\Psi(u) = A \frac{\sin(w_\alpha u)}{w_\alpha u}$$

such as shown in Fig. 8.

Since the electric field distribution at the end of a single-mode waveguide does not look like a the function in Fig. 8, we can not achieve an ideally efficient coupler. However, Dragone has shown that a highly efficient coupler can still be implemented. He assumes for simplicity that the input distribution looks like

$$\Psi(u) = A \cos(w_\alpha u)$$

such as that shown in Fig. 9.

By taking the Fourier transform of the function in Fig. 9, we can see what the shape will be at the output array. The transformed function is

$$\Phi(w) = A \left(\frac{\sin(w + w_\alpha)}{w + w_\alpha} + \frac{\sin(w - w_\alpha)}{w - w_\alpha} \right)$$

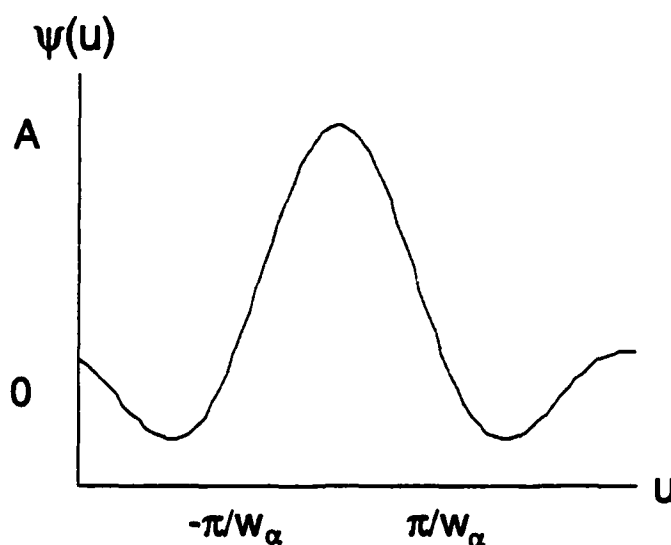


Figure 8. The necessary shape of the electric field distribution at the input in order to achieve a rectangular shape at the output.

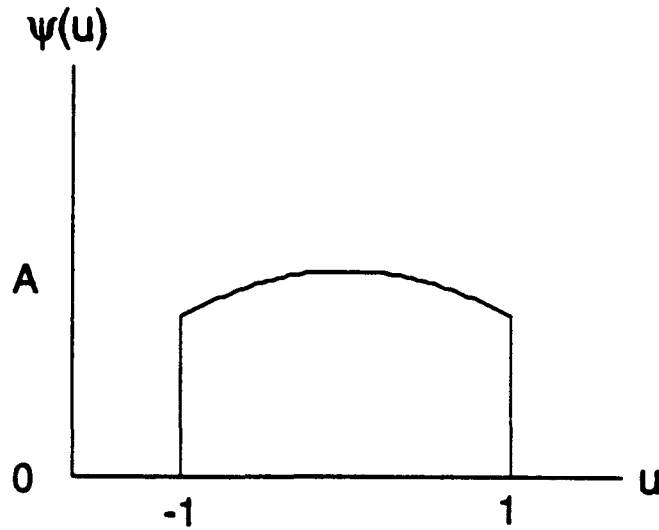


Figure 9. Assumed electric field distribution at the end of a single-mode waveguide entering the free-space region. In this approximation no field exists outside the waveguide.

as shown below in Fig. 10. It can be demonstrated that maximum efficiency realizable for our coupler geometry (as in Fig. 1), given an input distribution such as in Fig. 9, occurs when

$$w_{\alpha} = \frac{\pi a \sin \alpha}{\lambda} = 0.9 \quad (16)$$

Equation (16) provides us with the key element we need to construct our design equations. For convenience the coupler geometry of Fig. 1 is presented again in Fig. 11.

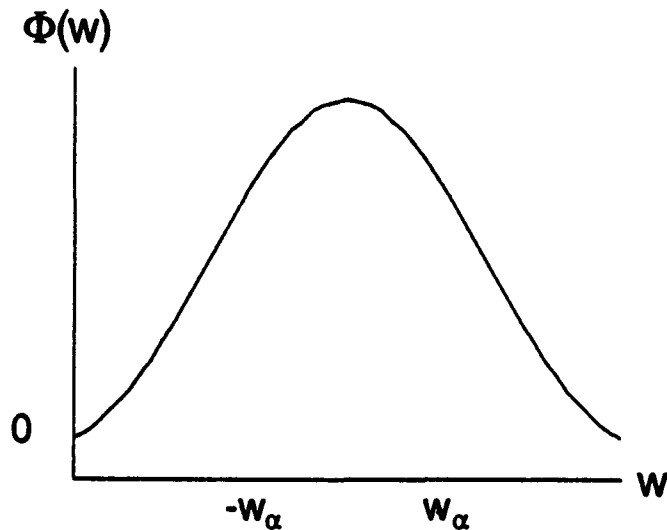


Fig. 10. Resulting shape of electric field distribution at the output array, given an input function such as that displayed in Fig. 9.

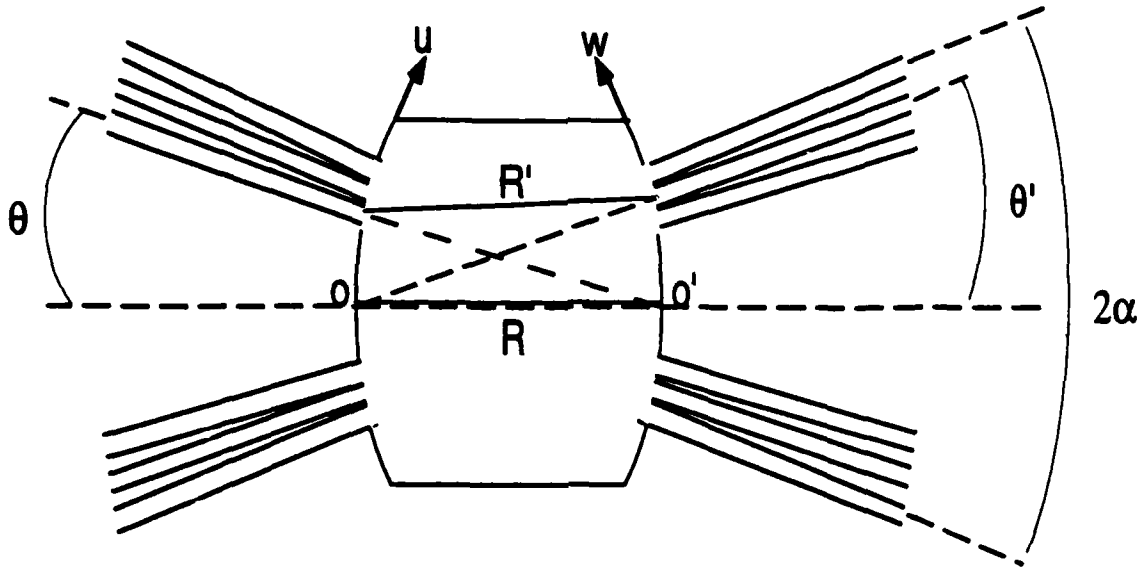


Figure 11. Schematic plan view of a star coupler. R is the distance between the two array centers. R' is the distance between an input and an output aperture located at an angle of θ and θ' respectively. 2α is the angular extent of each array of N waveguides and a is the spacing between waveguides at the free-space boundary.

The variables involved are

R = radius of curvature

α = half the angular extent of waveguide array

N = number of waveguides in array

a = spacing between waveguide centers at free-space boundary

λ = wavelength of operation

Since the waveguides are touching side-by-side at the free-space boundary the spacing between waveguide centers is equal to the waveguide width, and we can write

$$N = \frac{2\alpha R}{a} \quad (17)$$

Equations (16) and (17) are the design equations. When implementing the design we will choose values for N , a , and λ . Our choices for those variables depend on the desired capacity and operating wavelength of the coupler, as well as the waveguide dimensions necessary for efficient fiber-to-waveguide coupling. For the implementation of our initial designs we chose

$$N = 10$$

$$a = 7.5 \mu\text{m}$$

$$\lambda = 1300\text{nm}$$

The remaining two variables (representing the size and angular extent of the coupler) are determined by these choices and (16) and (17), such that

$$\alpha = \sin^{-1} \left(\frac{0.9\lambda}{\pi a} \right)$$

$$R = \frac{aN}{2\alpha}$$

A final choice must be made before the coupler is completely designed: what geometry shall be used to determine the waveguide path out from the central region to the position on our substrate where they will be coupled with optical fiber. Using s-bends is one possible method. However, to avoid the losses and extra complexity associated with s-bends, we chose to bring our waveguides straight out from the central region. The overall length of the coupler then is dependent on the final spacing needed between waveguides to allow insertion of optical fiber. Our solution is described in more detail in the following section.

Fabrication of Photomask

We have implemented a mask design in AutoCad which has been fabricated by the Applied Image company. The mask is 4" X 4" and consists of chrome patterned on glass. There are several features present on the mask including a 2 μm grating, several sets of 7.5 μm waveguides of varying length, two electro-optic switch structures, and two 10 x 10 star couplers. Only the couplers will be described in detail at this point.

For these couplers we have chosen

$$\begin{aligned} N &= 10 \\ a &= 7.5 \mu\text{m} \\ \lambda &= 1300\text{nm} \end{aligned}$$

requiring that

$$\begin{aligned} \alpha &= 2.846^\circ \\ R &= 754.8 \mu\text{m} \end{aligned}$$

In addition, we have decided to bring the waveguides straight out from the central region, with no bends. Since there are 10 waveguides evenly arrayed in a range of 2α , the angle between each waveguide will be approximately 0.5695° . We require 250 μm of space between waveguides at the fiber-to-waveguide interface to allow room for our alignment structures, and to coincide with industry standard spacing on optical fiber ribbons. Therefore each waveguide is 24.396 mm in length. A diagram of the alignment structures is presented in Fig. 12.

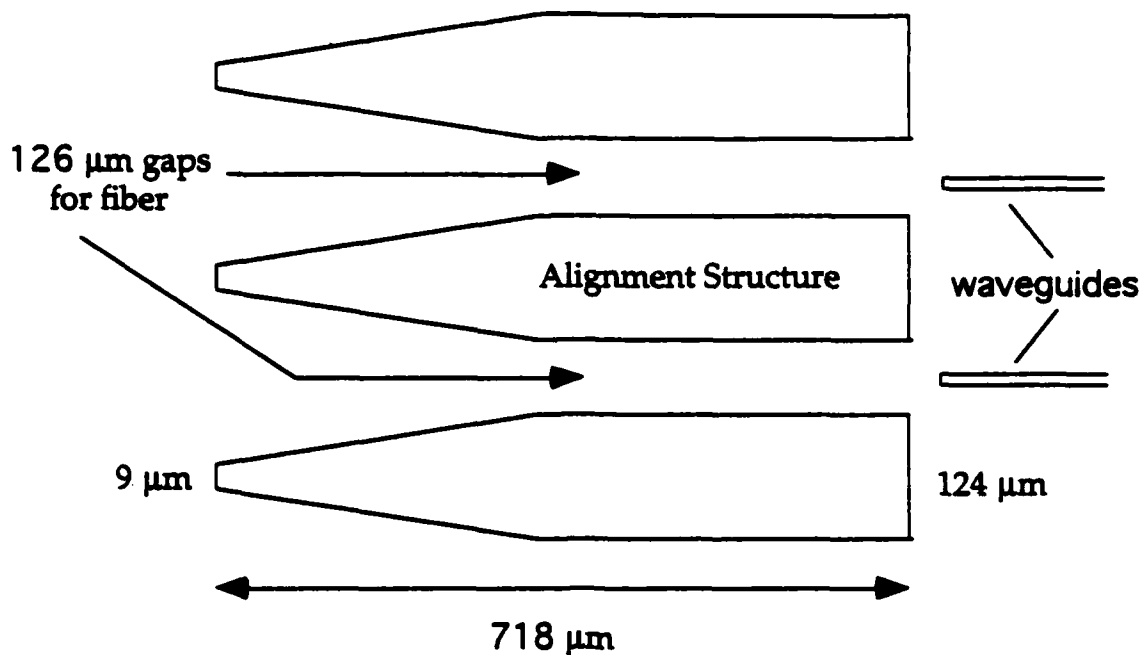


Figure 12. Diagram of alignment structures. Note that for the actual coupler the waveguides are not parallel, but separated by an angle of 0.5695° . The two optical fibers which slide in between the structures will also be aligned at that angle. This orientation is built into the alignment structures, though not shown in this diagram.

Although quite usable for future work, the photomask has a number of imperfections, and we do not recommend Applied Image for further work at this time. However, the main cause of problems with the quality of the mask lie in our use of AutoCad to produce the schematics. The various data file formats available to AutoCad are not easily converted to the data file format required by mask houses. We hope in the future to move to a more versatile CAD package.

Now that we have a photomask with a coupler pattern, the next step is to prepare our polymers so that they will be suitable for the fabrication single-mode waveguides. The following section concerns our work on that problem.

Refractive Index Measurement and Tailoring

Introduction

We have been using two kinds of photosensitive monomer blends to fabricate multimode and single-mode polymer waveguides for our research. The primary resins are a high-index aromatic acrylated epoxy (Ebercryn 600) and a low-index aliphatic urethane dimethacrylate (Ebercryn 4883). A diluent (OTA 480) and photoinitiator (Irgacure 184) make up the remaining ingredients of both monomer blends.⁴ Upon the initiation of this contract many important characteristics of the monomers as well as the cured polymers were not well known. An in depth characterization of the polymers is being conducted and will be presented in the final report. However, in this section we present index of refraction measurements of the high and low-index polymers as well measurements of polymer blends made of mixtures of the two primary monomers.

The need for accurate measurement of the indices of our polymers is rooted in our desire to create a *single-mode* star coupler. Whether or not a waveguide will operate single-mode for a specific input wavelength is strongly dependent on two interrelated factors: the waveguide dimensions and the difference in index, Δn , of the guiding and cladding layers. Since we desire that the mode-field of our waveguides match the mode-field of a standard optical fiber, we have chosen that our waveguides be $7.5 \times 7.5 \mu\text{m}$ in dimension.

Using the effective index method we can calculate the difference in index of refraction required to keep our waveguides operating single-mode.⁵ Choosing a cutoff wavelength of $\lambda_c = 1100 \text{ nm}$ and a waveguide thickness of $a = 7.5 \mu\text{m}$, we find that for $0 < \Delta n < 0.0016$ our waveguides will be single-mode at an operating wavelength of 1300 nm . It is clear from this result that we need to know the index of refraction of our polymers and polymer blends with an accuracy on the order of 10^{-3} to be able to implement the precise Δn needed for our waveguides.

Fabrication of Monomer Blends

The fabrication of the monomer blends which will be spun on to silicon and photo-patterned follows this procedure. While heating the primary resins for 30 minutes at 50°C to thin them, 2 g of the photoinitiator is completely dissolved in 60 g of diluent. Then 140 g of either high or low-index resin and the diluent/photoinitiator mixture is stirred at $60\text{-}70^\circ\text{C}$ for 4-5 hours. The result is a batch of monomer which photocures into a either a high or low index polymer, depending on which resin is used. These two possible batches represent the high and low end of the range of indices that we can create. By mixing a varying percentage (by weight) of high-index and low-index monomer at $60\text{-}70^\circ\text{C}$, we can obtain values of the index in between the two bounds.

⁴ T. S. Barry, *et al.* "Efficient Optical Fiber-To-Waveguide Coupling Suitable for Passive Alignment," 43rd Conf. Electric Components & Technology, pp. 1139-1142, Orlando, Florida, June 2-4, 1993.

⁵ Hiroshi Nishihara, *et al.* Optical Integrated Circuits. (McGraw-Hill, New York, 1989).

Refractive Index Measurement

For the refractive index measurement of our polymer blends, commercial refractive index liquids⁶ with indices of 1.490, 1.500, 1.510, 1.520 and 1.530 are used for reference. First, monomer blend is spun on a silicon substrate at 2000 rpm. The sample is then photo-cured under a photomask in order to fabricate a well structure, as depicted in Fig. 13. Next, the well structure is filled with refractive index liquid of a suitable index and then covered by a small piece of cover glass.

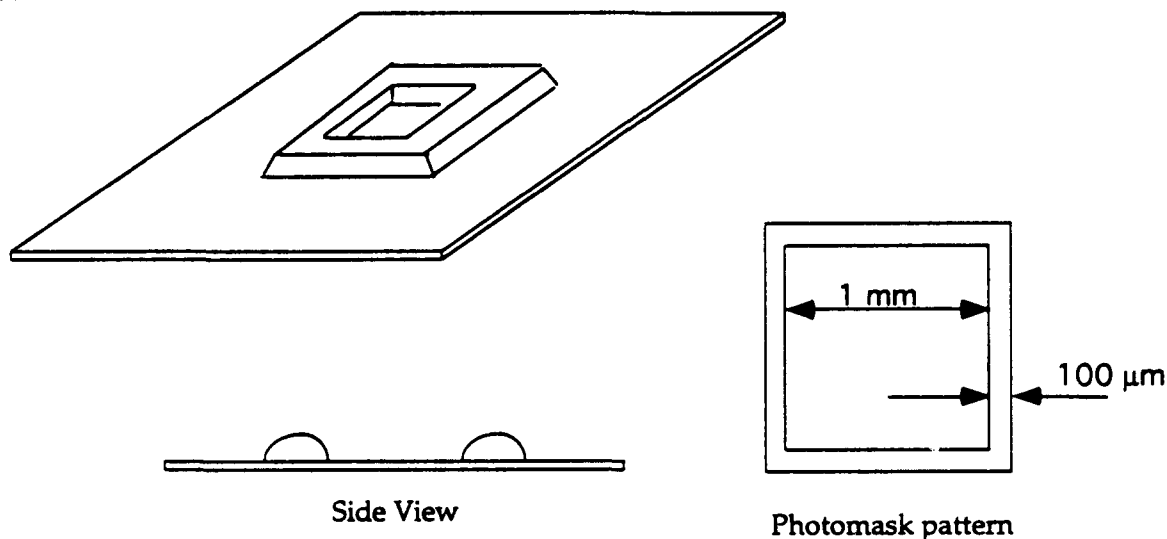


Figure 13. Polymer well structure and photomask pattern. In order to better distinguish the shift of Michelson fringes, the walls of the well structure were intentionally sloped.

The refractive index of the polymer used to make the well structure can now be obtained by measuring index difference Δn between the polymer and the refractive index liquid. This can be accomplished by viewing the sample through a microscope with an attachment that functions as a Michelson interferometer. Fig. 14 presents a side-on view of this setup.

The interference fringes will be uniform for a sample which is optically uniform and flat. If the sample is not optically uniform, the fringes are shifted corresponding to the difference of the optical path length $\Delta n \times d$ as shown in Fig. 15, where d is the height of sample.

$\Delta n \times d$ is given by

$$\Delta n \times d = \frac{a\lambda}{2b}$$

where a is the shift of the interferometric fringe, b is the space between each fringe, and λ is the wavelength of the light source of the interferometer. Consequently Δn can be obtained from

$$\Delta n = \frac{a\lambda}{2bd}$$

⁶ These liquids (Series A) are supplied by R. P. Cargille Laboratories, Cedar Grove, NJ 07009.

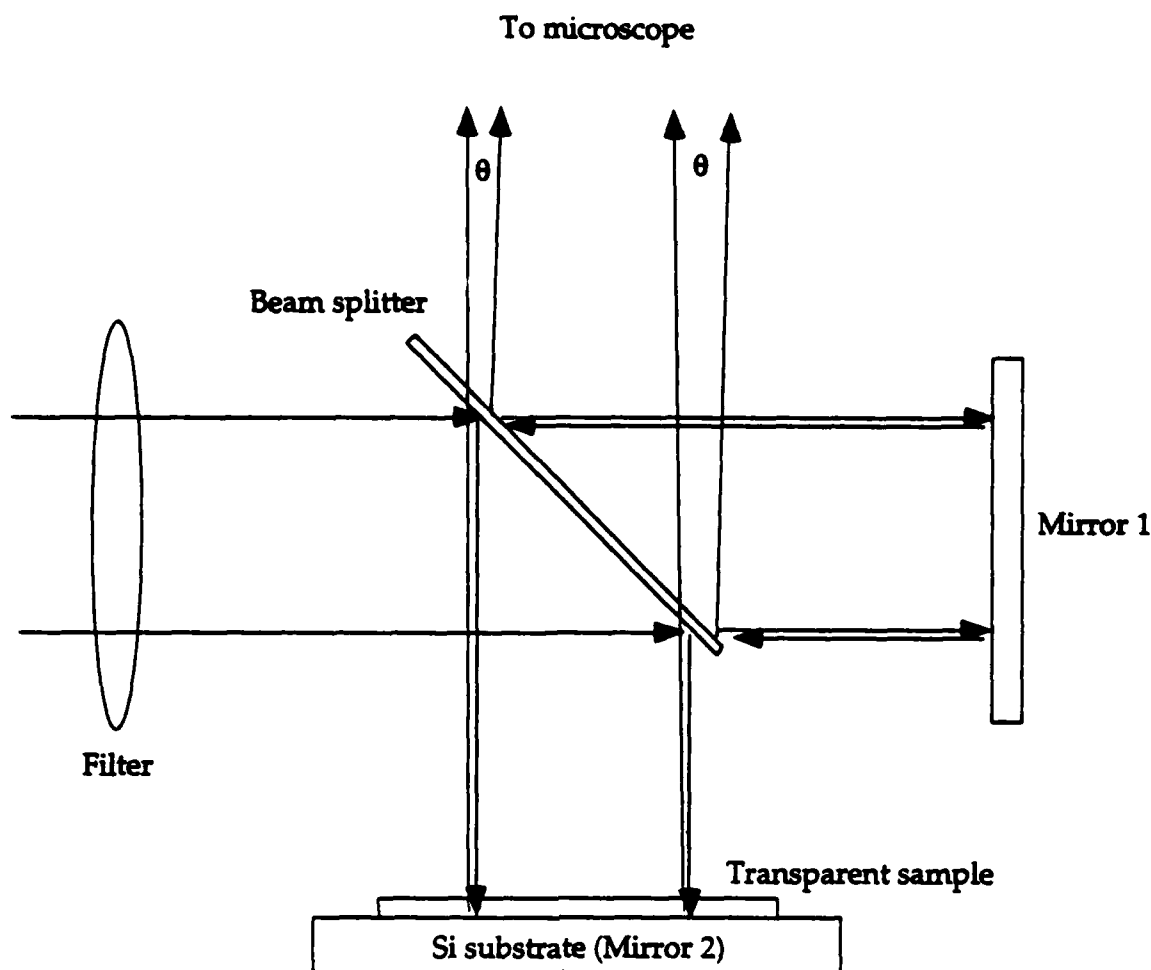


Figure 14. A Michelson interferometer. Light reflected by mirror 2 interferes with light reflected from mirror 1 to produce fringes superimposed on an image of the sample.

In our experiment d was measured by a profilometer for each sample, and λ was 0.589 nm (Na D line filter). A typical interferogram is shown below in Fig. 16.

The results of a series of refractive index measurements of polymer blends is shown in Fig. 17.

These results indicate that our single-mode waveguides should be fabricated of a polymer containing 97% low-index monomer and 3% high-index monomer (assuming $\Delta n = 0.0016$). We use pure low-index monomer for our cladding layer because it is closely matched to the index of our glass fiber, and will reduce Fresnel reflection when coupling light from fiber to waveguide. Current work is being done to refine our ability to produce acrylic waveguides with the correct single-mode dimensions, after which a coupler can be fabricated and tested. Such tests will require efficient and reproducible fiber-to-waveguide coupling. The following section refers to work addressing that problem.

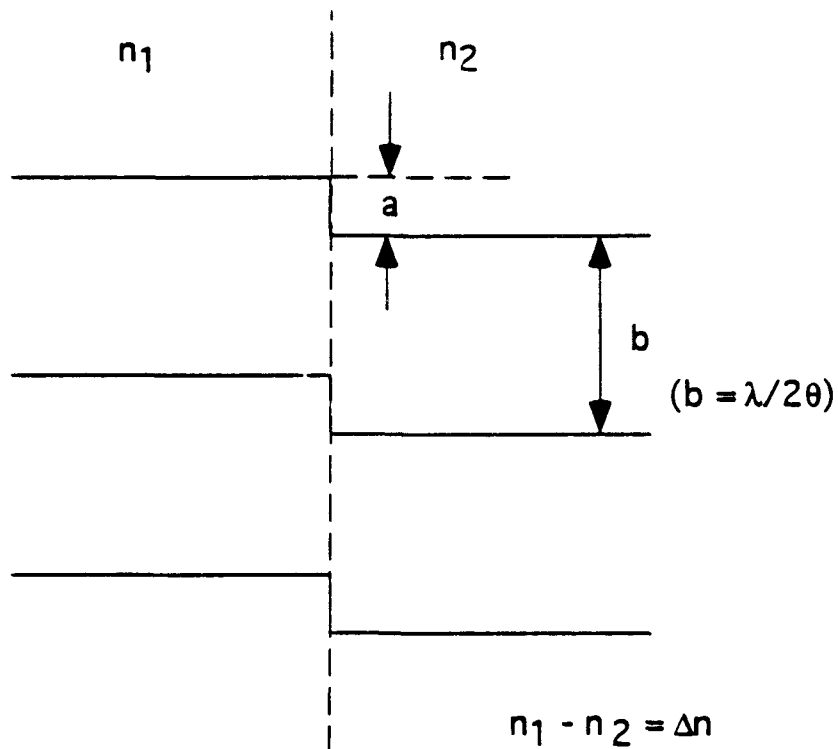


Figure 15. An example of interference fringes for a hypothetical sample with differing indices on the left and right.



Figure 16. Typical interferogram. In the middle, showing curved fringes, is a section of the well structure. The material on either side is index measurement liquid with index of 1.490. $a/b = 0.25$ and $d = 16.9 \mu\text{m}$, therefore $\Delta n = +0.0043$ then $n = 1.490 + 0.0043 \approx 1.494$.

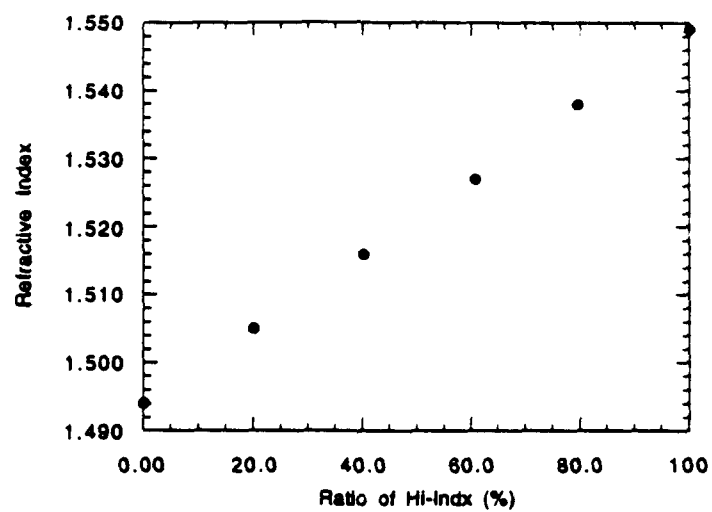


Figure 17. Graph of refractive index as a function of the ratio of high index monomer in the polymer blend being measured.

D-fiber Fabrication and Testing

In a recent paper presented by our group at the 43rd Electronic Components & Technology Conference, June 1993, we introduced a new coupling concept wherein the same processing steps used to fabricate our star coupler are used simultaneously to fabricate polymer *alignment* structures. These structures are located at the ends of the input and output waveguides of the coupler to aid in the accurate positioning of optical fibers (see Fig. 12).

These alignment structures require that the optical fibers be fabricated with D-shaped transition regions near their coupling ends, in order to correctly match the core of the fiber to the core of the waveguide. The D-fiber fabrication technique consists of lapping away the cladding layer of an optical fiber, leaving a flat surface just outside the core.

For further information on the alignment structures and D-fiber, we refer the reader to the ECTC paper (T. S. Barry *et al.*, "Efficient Optical Fiber-To-Waveguide Coupling Suitable for Passive Alignment.") which has been included with this report.

Conclusion

In this report we have presented our progress to date in several areas: the design and fabrication of an $N \times N$ star coupler, the measurement and tailoring of the index of refraction of our polymer blends, and the fabrication of D-fiber. We have succeeded in developing design equations for the star coupler and have used them to fabricate a photomask with which to pattern a coupler. In addition, we have shown the ability to measure and tailor the index of refraction of our polymer blends accurately enough to allow fabrication of single-mode waveguides. Finally, we have referred to our highly successful work in the area of passive fiber-to-waveguide coupling.

During the next six months we will apply the techniques and knowledge presented in this report to the fabrication, testing, and delivery of a 10×10 star coupler.

Part II – Final Report

Single-Mode D-Fiber

The concept of using optical fiber with a D-shaped cross-section ("D-fiber") in applications where it is useful to access the evanescent field of the guided mode has been explored by several authors over the last decade. These works include fiber-to-fiber directional couplers,^{7,8} fiber-to-waveguide directional couplers,⁹ grating reflectors,^{10,11} wavelength-selective devices^{12,13} and optical modulators.¹⁴ More recently, we have found that D-fiber also presents some interesting utility relating to passive coupling between standard circular cross-section optical fiber and planar polymer optical waveguides.¹⁵

Although the idea of using D-fiber to achieve efficient coupling between fiber and waveguides was suggested earlier by Dyott and Schrank,¹⁶ the viability of applying this concept to not only a coupling technique but a *passive* coupling technique was shown only recently.⁹ This approach consists of utilizing the flat side of the D-shaped cross-section to assist the alignment in one transverse direction while integrated alignment ways are provided for the remaining transverse direction. The D-fiber is fabricated within a standard single-mode optical fiber by use of a cylinder lap applied to a 3 mm long region of the fiber. Low coupling losses (0.25 dB) have been obtained using this technique to couple multimode fibers and multimode waveguides.¹⁷ An important aspect of this work, which utilizes not only D-fiber but also self-aligning ways, is that one can thereby extend this approach to the interconnection of parallel arrays of waveguides with fiber

-
- ⁷ R.A. Bergh, G. Kotler and H.J. Shaw, "Single-mode fibre optic directional coupler," *Electron. Lett.*, vol. 16, pp. 260-261, 1980.
 - ⁸ G. Schöner, E. Klement, G. Schiffner and N. Douklias, "Novel method for making single-mode optical fibre directional couplers," *Electron. Lett.*, vol. 18, pp. 566-567, 1982.
 - ⁹ M. Zhang and E. Garmire, "Single-mode fiber-film directional coupler," *J. Lightwave Technology*, vol. LT-5, pp. 260-267, 1987.
 - ¹⁰ W.V. Sorin and H.J. Shaw, "A single-mode fiber evanescent grating reflector," *J. Lightwave Technol.*, vol. LT-3, pp. 1041-1043, 1985.
 - ¹¹ C.J. Rowe, I. Bennion and D.C.J. Reid, "High-reflectivity surface-relief gratings in single-mode optical fibres," *IEE Proc.*, vol. 134, Pt. J, pp.197-202, 1987.
 - ¹² C.A. Millar, M.C. Brierley and S.R. Mallinson, "Exposed core single mode fibre channel dropping filter using a high index overlay waveguide," *Opt. Lett.*, vol. 12, pp-284-286, 1987.
 - ¹³ W. Johnstone, G. Thursby, D. Moodie, R. Varshney and B. Culshaw, "Fibre optic wavelength channel selector with high resolution," *Electron. Lett.*, vol. 28, pp. 1364-1365, 1992.
 - ¹⁴ W. Johnstone et al., "Fibre optic modulators using active multimode waveguide overlays," *Electron. Lett.*, vol. 27, pp. 894-896, 1991.
 - ¹⁵ T.S. Barry, M.H. Cordaro, R.R. Krchnavek, K. Nakagawa, C. W. Phelps and D.L. Rode, "Efficient optical fiber-to-waveguide coupling suitable for passive alignment," *43rd Electronic Components & Technology Conference*, Orlando, FL, pp. 1139-1142, June 1993.
 - ¹⁶ R.B. Dyott and P.F. Schrank, "Self-locating elliptically cored fibre with an accessible guiding region", *Electron. Lett.*, vol. 18, pp. 980-981, 1982.
 - ¹⁷ T. S. Barry, D. L. Rode, M. H. Cordaro and R. R. Krchnavek, unpublished work.

ribbon assemblies important for bit-parallel digital communications. In the present paper, we extend this work to 8 μm -core single-mode fiber.

To fabricate single-mode evanescent-field devices from single-mode fibers and to address the much more challenging problem of applying the aforementioned passive coupling technique to single-mode structures, it is necessary to remove the cladding layer to within about one micron of the core with accuracy and reproducibility better than $\pm 1 \mu\text{m}$. It becomes clear therefore that an accurate measurement of the depth of the removed layer is essential in this case. One method to perform this measurement with good precision was described by Digonnet, Feth, Stokes and Shaw.¹⁸ It consists of monitoring the throughput attenuation occurring for light propagating in the fiber when a drop of refractive-index fluid is placed on the polished surface. Although it allows good accuracy, this method requires that the refractive index of the fluid be controlled precisely. Furthermore it does not provide for monitoring the core proximity while the cladding layer is in the process of being removed. On the other hand, the main purpose of this article is to describe an *in situ* monitoring technique for this task.

Theoretical Analysis

Consider a step-index optical fiber with a core radius a , cladding outside-diameter D , core refractive index n_1 and cladding refractive index n_2 . Since we use a cylinder lap to fabricate D-fiber, let the fiber be sectioned by a cylinder of radius R and length L , where R and L are both much larger than a and D . The cylinder axis is held perpendicular to the axis of the fiber, which we define as the z -direction. The depth of penetration of the cylinder into the fiber as measured from the point located at $D/2$ from the optical axis is called h , as depicted in Fig. 1. Monochromatic light of sufficiently small wavelength (λ , in vacuum) so that several modes propagate is launched into the fiber which has a value of $(n_1 - n_2)$ much smaller than unity so that all modes propagating within the fiber can be treated as linearly polarized modes.^{19,20} The problem therefore consists of how to evaluate the power flow carried by the propagating modes as a function of h . We use 633 nm light for monitoring purposes so that four propagating modes exist whereas the optical fiber in actual use for optical communications purposes is operated single-mode with 1300 nm light.

Although it is not as complete as an electromagnetic-wave treatment, applying a geometrical optics approach to this problem shows relatively simply that there are various cutoff depths associated with the various propagating modes. This in turn leads to cutoff of various modes at distinct values of the depth h . The surface of intersection between the fiber and the cylinder defines a gradual asymmetric tapered region along the z -direction. This transforms propagating modes into radiation modes for cylinder penetration depths beyond certain critical values that we relate to the cutoff penetration depth (h_c). Geometrical optics gives us a simple way to calculate h_c .

¹⁸ M.J.F. Digonnet, J.R. Feth, L.F. Stokes and H.J. Shaw, "Measurement of the core proximity in polished fiber substrates and couplers," *Opt. Lett.*, vol. 10, pp. 463-465, 1985.

¹⁹ D. Gloge, "Weakly Guiding Fibers," *Appl. Opt.*, vol. 10, pp. 2252-2258, 1971.

²⁰ A. Yariv, *Optical Electronics*, New York:HRW, 3rd edition, 1985, pp. 66-78.

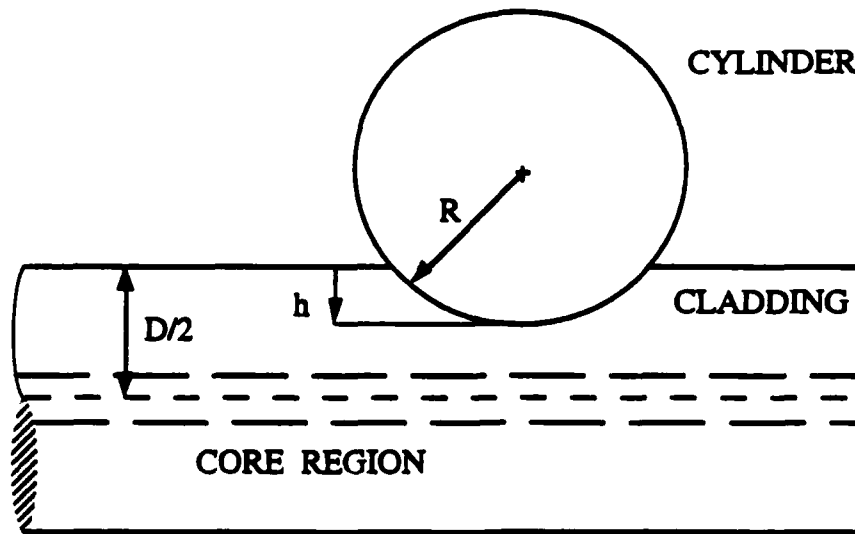


Figure 1. Schematic diagram of an optical fiber with core radi outside diameter D . The fiber is sectioned by a cylinder of radi

It has been shown for slab waveguides²¹ that each mode can be considered as a superposition of two zig-zag plane waves confined within the region of higher refractive index due to frustrated total internal reflection at the interface with the medium of lower refractive index, *i.e.* the cladding. Plane waves with angles of incidence at the interface such that the transverse eigenvalue conditions are satisfied are the only stationary modes that propagate along the structure. Therefore, each mode (TM or TE) in a slab waveguide has its own characteristic angle of incidence which always lies between the critical angle for frustrated total internal reflection (θ_{cr}) and 90° . This upper limit (90°) corresponds to the wave vector of the plane wave lying parallel to the z -axis. Furthermore, for slab waveguides where the propagating modes are weakly guided ($n_1 - n_2 \ll 1$), a significant amount of the electromagnetic energy resides within the cladding layer. To take this characteristic into consideration for the slab-waveguide geometrical-optics model, each mode is considered to possess its own effective width, which is calculated by adding the effective enlargement caused by the Goos-Hänchen shift^{15,22,23} to the physical width of the slab.

We assume that the above geometrical-optics treatment described for a slab waveguide can be applied to a cylindrical step-index optical fiber which allows the propagation of only a few linearly polarized modes. Therefore, each mode of radial order m and azimuthal order l has a particular meridional angle of incidence θ_{lm} and a particular effective mode radius a_{eff} given as follows.

$$\theta_{lm} = \sin^{-1}(\beta_{lm}/kn_1) \quad (1)$$

²¹ H. Kogelnik, "Theory of Optical Waveguides," T. Tamir (Ed.), *Guided-Wave Optoelectronics*, Berlin: Springer-Verlag, 2nd edition, 1990, pp. 7-20.

²² J.E. Midwinter, *Optical Fibers for Transmission*, New York: John Wiley & Sons, 1979, pp. 33-38.

²³ K. Yasumoto and Y. Oichi, "A New Evaluation of the Goos-Hänchen Shift and Associated Time Delay," *J. Appl. Phys.*, vol. 54, pp. 2170-2176, 1983.

$$a_{\text{eff}} = a + x_s(\theta_{\text{lm}}) \quad (2)$$

Here, β_{lm} is the propagation constant for the (lm) mode, x_s is the enlargement caused by the Goos-Hänchen shift and k is the wave number in vacuum ($k=2\pi/\lambda$). To obtain the enlargement of the radius for each mode as a function of the modal propagation constant, we use the expressions derived for slab waveguides as presented in the literature.¹⁵ Since n_1 is approximately equal to n_2 , TE and TM modes have nearly the same enlargement, the enlargement being obtained from the following equation.

$$x_s = 1 / \{k(n_1^2 \sin^2 \theta_{\text{lm}} - n_2^2)^{1/2}\} \quad (3)$$

β_{lm} can be obtained from the analysis and graph of normalized propagation parameter β versus V (normalized frequency, or V-number) developed by Gloge.¹³

The effects of the cylinder on mode propagation can now be evaluated by examining what happens to the zig-zag propagating wave when the cylinder begins to intersect the modal region of radius a_{eff} . As depicted in Fig. 2, when the cylinder contacts the region at $r = a_{\text{eff}}$, the angle of reflection at this point becomes $\theta_{\text{lm}} - \phi_t$, where ϕ_t is the angle between the tangential plane to the cylinder surface and the z-axis. Following the ray trace after the first reflection, it impinges on the diametrically opposite interface with an angle of incidence $\theta_{\text{lm}} - 2\phi_t$ in relation to the normal to the interface. It is clear that the presence of the reflecting surface of the cylinder makes the angle of incidence move toward the critical angle.

We may now define the cutoff angle ϕ_c as the angle ϕ_t that causes $\theta_{\text{lm}} - 2\phi_t$ to equal θ_{cr} .

$$\phi_c = (\theta_{\text{lm}} - \theta_{\text{cr}}) / 2 \quad (4)$$

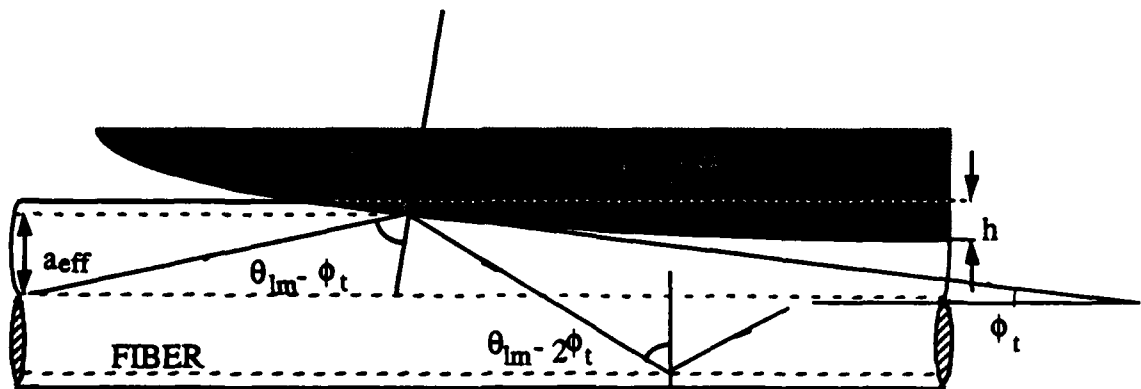


Figure 2. Ray-tracing diagram showing the stripping of higher-order modes caused by the sectioning cylinder. The modal angles of incidence are measured from the normal to the surface of the cylinder and to the core-cladding interface.

Since the cutoff angle is known from eq.(4) and mode calculations, the cutoff penetration depth (h_c) can be obtained through simple geometry from Fig. 2.

$$h_c = D/2 - a_{\text{eff}} + R(1 - \cos\phi_c) \quad (5)$$

As an example, consider monochromatic light with $\lambda = 633$ nm propagating in a step-index optical fiber with $D = 124$ μm , $a = 4$ μm , $n_1 = 1.4629$ and $n_2 = 1.4580$. The optical fiber is sectioned by a cylinder with $R = 19.85$ mm. Since $V = 4.75$, there are four linearly polarized modes which are allowed to propagate; LP_{01} , LP_{11} , LP_{21} and LP_{02} . By using eqs.(1) through (5), after β_m has been found and being aware of $\theta_{cr} = 85.3^\circ$ for the given core and cladding refractive indices, the cutoff depth for each mode can be calculated. The results are shown in Table I.

Despite being somewhat simple, the above model shows that the two higher-order modes present cutoff penetration depths that lie inside the cladding layer, which means these two modes are stripped by the cylinder just before it penetrates into the core region. Indeed, if one monitors the optical power propagating in the optical fiber beyond the sectioned region as a function of the penetration depth h , and assumes that each mode carries the same amount of power, one should expect the optical power to drop from its reference value, set at $h = 0$ μm , down nearly 3 dB when h is greater than 56.5 μm , continuing to decay to around 6 dB when the cylinder penetrates 1.4 μm into the core region. Based upon this analysis, it is fair to conclude that it should be possible to measure with this type of *in situ* monitoring the position of the cylinder within a range from 1.5 μm away from the core-cladding interface to 1.5 μm into the core region.

One might also consider the case of *in situ* monitoring using single-mode operation, *i.e.* 1300 nm wavelength instead of 633 nm. To make this comparison, we assume light propagation in the same optical fiber sectioned by the same cylinder. The cladding layer is made from pure silica such that $n_2 = 1.4468$ and we expect the difference between n_1 and n_2 is independent of the wavelength. It results that $n_1 = 1.4517$ and $V = 2.30$, which implies that the structure allows only one mode of propagation (LP_{01}). After β_{01} has been obtained, from eqs.(1) - (5), we find that $\theta_{cr} = 85.3^\circ$, $\theta_{01} = 86.7^\circ$, $a_{\text{eff}} = 6.4$ μm and $h_c = 57.1$ μm . In terms of output optical power, this result suggests that one should expect a rather strong and featureless attenuation characteristic at $h = 57$ μm which still would be 1 μm away from the core. Beyond this value, the attenuation of the output power might be too high to allow accurate monitoring of the cylinder position h . On the other hand, operation with a few somewhat-low-order modes provides distinctive features in the attenuation characteristic *versus* h which can be monitored so as to attain the desired ± 1 μm precision.

Experimental Results

The optical fibers used in this work are step-index single-mode (Siecor SMF-21) with cladding diameter 124 μm , mode-field diameter 8.5 μm , cutoff wavelength 1.25 μm and loss of 0.4 dB/km at 1.3 μm .²⁴ The cladding and core diameters imply that it is necessary to remove nearly 58 μm of cladding layer to reach a position of ± 1 μm from the core-cladding interface.

²⁴ R.K. Boncek, "High-Performance LEDs for Fiber-Optic Loop-Plant and LAN Communication Systems," D.Sc. dissertation, Washington University, St. Louis, MO, May 1990.

Removal of the desired portion of the cladding layer is carried out by means of mechanical lapping with a large-diameter cylinder which forms a groove through the fiber while the axis of the lapping cylinder is held perpendicular to the optical axis of the fiber. The lapping procedure is performed on a modified Philtec Model 2015-C sectioner²⁵ consisting of a rotating polymer spindle dressed with 3 μm (nominal) diamond particles held in a polymer coating. The fiber is held in a glass holder containing a 132 μm wide slot on one face. The glass holder, in turn, is secured in a clamping chuck. The lapped optical fibers are mounted in the slots with petroleum-distillate black wax (Apiezon) which is optically strongly absorbing. The slots are about 55 μm deep. The lapping spindle is 19.85 mm in radius and its rotational speed is maintained at 1625 RPM. Along with the steady rotational motion of the spindle, the chuck is also periodically (sinusoidally) displaced over a maximum range of 2 mm with a period of three seconds along a direction parallel to the axis of the spindle. The pressure between the chuck and the lap is controlled by setting the electric current passing through an electromagnet which presses the chuck against the spindle. Glycerol is used as the lapping coolant.

Two techniques are used to measure the depth of the lapped groove (h) after the lapping is completed, *i.e.* *ex situ* methods. One, the arcuic trigonometric method,¹⁹ consists of calculating h from the measured length of the major axis of the ellipse which is figured onto the surface of the fiber. This calculation is possible when the effective radius of the spindle is known and constant while lapping is performed, which may be dependent upon deformation due to the large pressures involved (see below). For these calculations, we assume the undeformed radius. The other is to measure, by optical microscopy, the dimensions of the cross-sections of the D-shaped fiber ends after cleaving near the center of the lapped region. Discrepancies between data obtained by these two methods appear to amount to somewhat less than 1 μm , probably limited by the precision of optical microscopy.

By measuring lapped depth h versus time under conditions of lapping pressure generally greater than about 1500 psi, we determined instantaneous lapping rates. For elapsed times of 20 sec and 1800 sec, we found lapping rates of $1.4 \pm 0.3 \mu\text{m/s}$ and $0.013 \pm 0.004 \mu\text{m/s}$. It is important to mention that before each lapping procedure the spindle is redressed in the same manner while trying to keep constant the initial value of the thickness of the diamond layer. We also used the same slot on the same glass holder to mount and lap the fibers one at a time. From these lapping rate values it is possible to see the strong reduction of the lapping rate with time as well as the average time to remove 58 μm of cladding material, which is fifteen to thirty minutes under these conditions.

To examine how the initial thickness of the diamond layer affects the lapping rate, we performed some consecutive laps without redressing the spindle. We observed that if the area of contact on the spindle was already used in a previous lapping process, the lapping rate can decay to as little as one-half of the value compared to when the spindle is redressed after every lapping procedure.

²⁵ Philtec Model 2015-C Sectioner, Operation and Maintenance Manual, Philtec Instrument Co. Philadelphia, PA 19129, 1981.

The oscillating movement of the chuck parallel to the axis of the spindle ameliorates nonuniform wear of the diamond layer and contributes to planarity of the lapped interface.

Another important issue in this process is the depth of the slots on the glass holder. If their depth is greater than the diameter of the fiber minus the desired penetration depth, the spindle will reach the glass holder during the latter stages of the lapping process. This, in turn, strongly increases the area of contact, decreasing the pressure and consequently the lapping rate.

The lapping rate decays as lapping proceeds and it also depends on pressure. Although these characteristics are always present when glass is mechanically polished with a viscoelastic lap covered with fine abrasive particles,²⁶ the present process presents some peculiarities. Since the depth of the slots on the glass holder is nearly equal to the radius of the optical fiber, the area of contact between the cylinder lap and the optical fiber is set by the force due to the electromagnet for groove depths up to nearly 60 μm . Recalling that the diameter of the fiber and the radius of the spindle are 124 μm and 19.85 mm, and noting that the force set by the electromagnet is around 100 gm force, it is possible to estimate that lapping pressures in excess of 1500 psi are present during the lapping process, being larger initially and trailing off to smaller values as the area of contact increases. The pressure is estimated from the 100 gm force and the ellipsoidal lapping area which measures 124 μm in width and 3.00 mm in length when $h = 58 \mu\text{m}$ for the finished lapped groove.

The pressure and lapping rate decay because the surface of contact increases as the spindle penetrates further into the fiber as one should expect from the geometry of the problem and the kinetics of polishing glass.¹⁹ Additional reduction of the lapping rate results because the diamond particles are worn and removed from the spindle surface at a rate depending on pressure, relative velocity, the materials of the spindle and the dressing solution. The latter characteristic makes the lapping rate sensitive to the initial thickness of the diamond dressing layer.

The optical quality of the lapped surface is evaluated by Michelson interferometry with 589 nm light (NaD line). An interferogram of the lapped surface of a single-mode optical fiber is shown in Fig. 3. The sharpness of the fringes shows that the surface is smooth to within 60 nm (approximately $\lambda/10$). It is pertinent to point out that this good surface quality was obtained with a nominal diamond particle size of 3 μm . This quality, aside from the particle size, can be explained by the high value of the Young's modulus of the fiber material, which results in shallow penetration of particles into the lapped surface even with pressures as large as 1500 psi due to their being suspended in a thick, compliant polymer binder.

Finally, due to the high values of lapping pressure and velocity, the lapping mechanism is thought to be predominantly mechanical. Keeping the pressure at about 1500 psi and with the same relative velocity, but using water as a coolant instead of glycerol, the lapping rate and surface quality are found to be very similar to the results obtained with glycerol. This leads us to believe that possible chemical reactions²⁰ between coolant and silica do not play a significant role.

²⁶ L. M. Cook, "Chemical Processes in Glass Polishing," *Journal of Non-Crystalline Solids*, 120, pp.152-171, 1990.

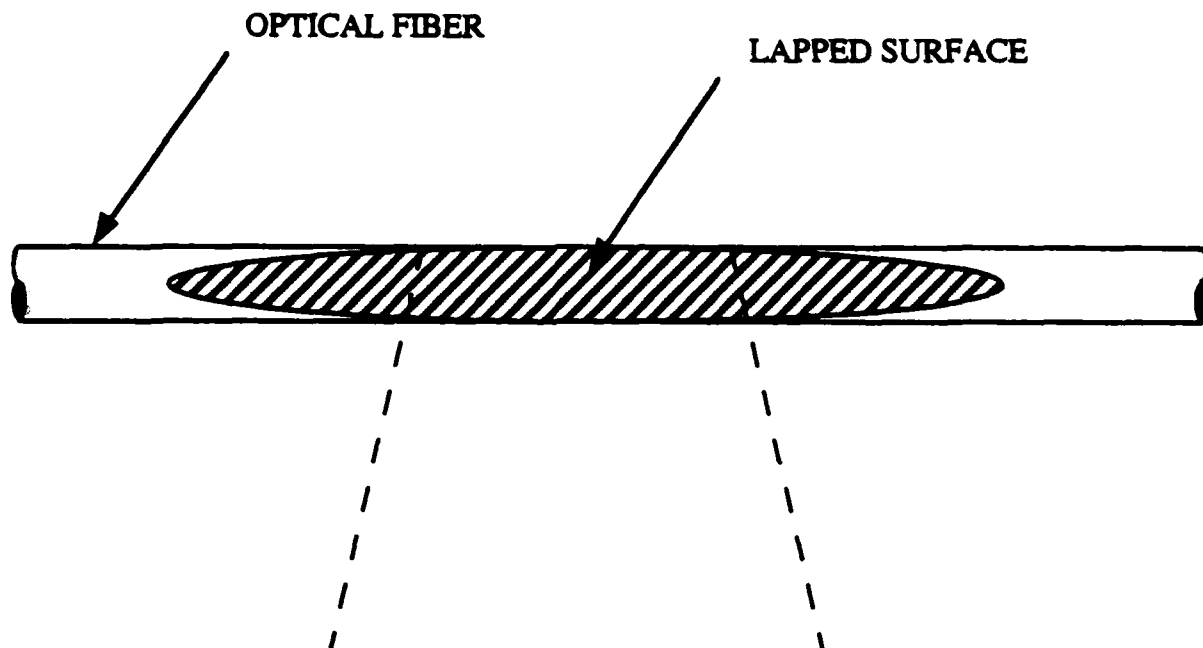


Figure 3. Michelson interferogram (NaD illumination) showing the surface quality of the lapped region of an optical fiber. The fiber is mounted with black wax in a groove on a glass holder. The region covered by the fringes measures $124\text{ }\mu\text{m}$ by about 1.53 mm . The lapped surface is slightly convex (two fringes, or $0.589\text{ }\mu\text{m}$) due to deformation of the cylinder during the high-pressure lap.

In order to reliably achieve $\pm 1\text{ }\mu\text{m}$ precision, we found it necessary to include *in situ* optical monitoring, which is described in the next section. The need for this kind of monitoring arises due to accuracy and repeatability requirements which must be maintained independently of the way the spindle is dressed, the depth of the slots on the glass holder, variations in the cladding diameter and the core position within the optical fiber itself, *i.e.* eccentricity.

The *in situ* monitoring technique consists of measuring changes in the throughput attenuation of launched light of a certain wavelength within the optical fiber while the lapping procedure is being carried out. The launched light is selected to excite not only the fundamental mode (LP_{01}) but also a few higher-order modes as well, *i.e.* LP_{11} , LP_{21} and LP_{02} . As can be seen in the theoretical analysis section, the spindle strips modes at different depths as it removes the cladding layer. Therefore, if the optical power coming out of the fiber during lapping is monitored, it is possible to accurately determine from subtle changes in throughput attenuation the distance between the lapped surface and the core-cladding interface.

The choice of the wavelength of the launched light depends upon certain characteristics of the fiber and the spindle. Excitation of too many modes is not desirable because steps and plateaus in the attenuation characteristic become too indistinct to perceive. It is also important to provide strong optical reflection at the fiber-spindle interface at the chosen wavelength by selecting the appropriate material for the coolant, the dressing solution and the surface of the spindle. In this work, we

found 633 nm light to be convenient for two reasons. One is that only four linearly polarized modes propagate in the optical fiber at this wavelength. The other is that the red-orange colored appearance of the surface of the spindle and the dressing solution we utilized for lapping provides the needed optical reflection.

A schematic diagram of the *in situ* monitoring set-up is depicted in Fig. 4. A 3mW He-Ne laser is used as a source of 633 nm light. A graded-index lens adapter is used to couple the collimated laser beam into the single-mode fiber which has a cutoff wavelength of 1250 nm. The optical power coming out of the other end of the fiber is used for the *in situ* monitoring. Each lapped fiber section measures approximately 2.0 m in length and the lapped portion is placed near the center of the fiber length. Two laser power meters (Spectra Physics and United Detector Technology) with Si pin photodiodes are used in the experiments. Both instruments are connected to a Macintosh computer by means of a MacLab analog-to-digital (A/D) converter (World Precision Instruments, Inc.) which is used for recording optical power as a function of time.

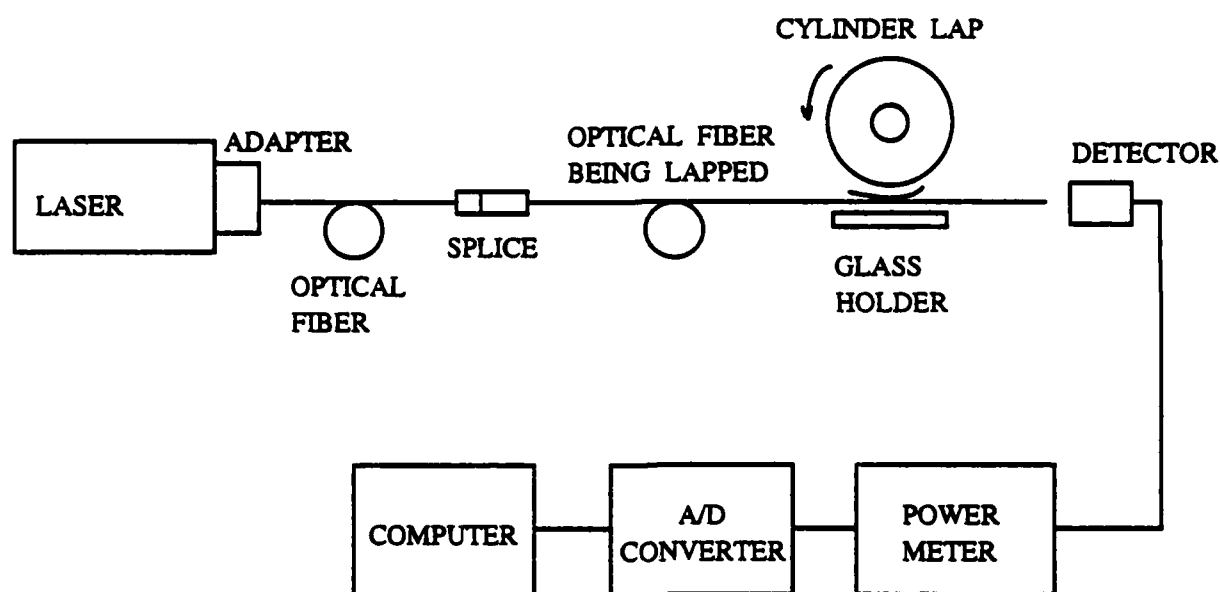


Figure 4. Schematic diagram of the *in situ* monitoring setup. A HeNe laser is used to excite a few linearly polarized modes in a step-index optical fiber with a cutoff wavelength of 1250 nm.

Fig. 5 shows a typical output power *versus* time characteristic obtained under the lapping conditions set out in Sec. 3.1. A single-pole low-pass filter (160 mHz cutoff frequency) is used at the A/D input to attenuate spurious signals related to the sinusoidal displacement of the chuck parallel to the axis of the spindle. These signals are found to increase as the spindle comes within a few microns of the core as one can infer from Fig. 5, *i.e.* the increasing vertical width of the trace beyond $t = 20$ min. This observation can be explained in terms of the sensitivity of the throughput attenuation to the periodically varying intimacy of contact between the fiber and the spindle as the chuck is displaced back and forth over the slight irregularities of the lapping surface of the spindle. By varying the lapping pressure *during* the lapping process, we find that the throughput attenuation

increases significantly as the pressure increases. Therefore, the monitoring and termination of the lapping process are based upon the *instantaneous maximum* values of attenuation which are caused by the closest contact between spindle and fiber.

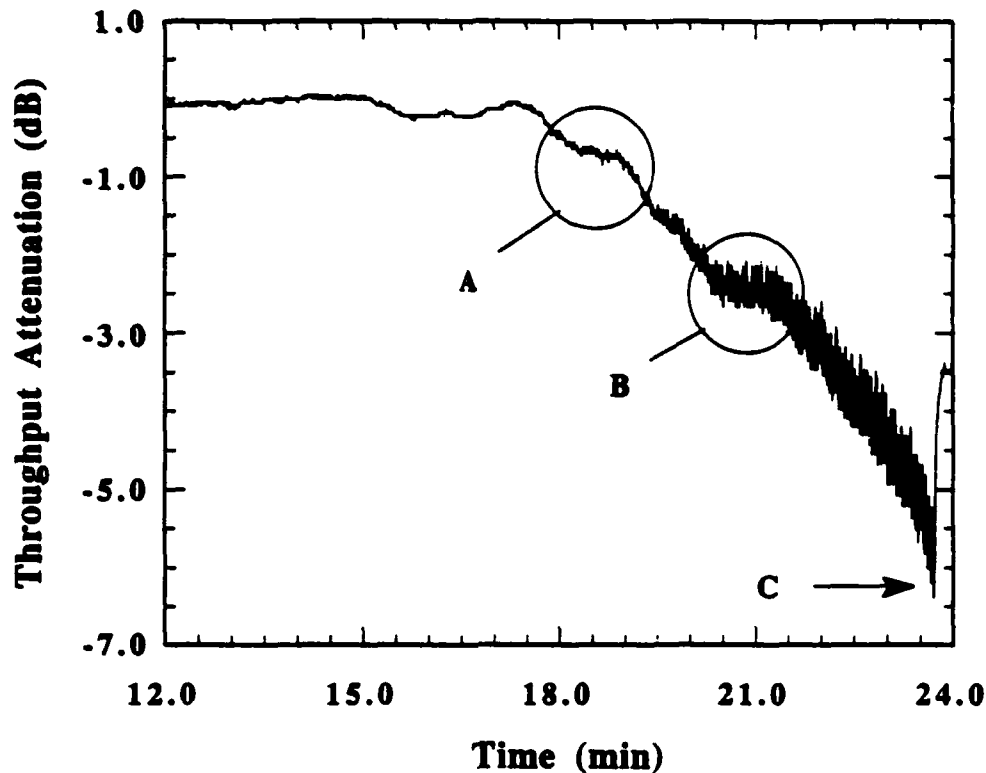


Figure 5. Typical throughput attenuation for 633 nm light *versus* lapping time for a single-mode fiber (for $\lambda = 1300$ nm) during cylinder lapping. Regions A and B indicate where the cylinder is within 2 to 3 μm and 1 to 2 μm from the core. Region C shows the instant when the lapping process is stopped at a throughput attenuation of -6.5 dB. The measured lapped depth in this case is 59.3 μm . After the cylinder is stopped and the pressure is released, the attenuation falls to values in the -3 to -4 dB range (see right side).

The starting instant in the curve of Fig. 5 is set when the rotating spindle contacts the fiber. The output power begins to decay after an elapsed time of 18 minutes. (Point A in Fig. 5.) A plateau at -2.7 dB is also noticeable. (Point B in Fig. 5.) After this point, the output power decays, presenting a downward concavity until the spindle rotation is turned off at -6.5 dB. (Point C in Fig. 5.) The measured lapping depth in this case is $h = 59.3 \mu\text{m}$. In order to characterize the lapping depths associated with points A, B and C, lapping is interrupted, stopping the spindle at levels of attenuation of -1, -3 and -6 dB and measuring the groove depth. This procedure shows depths within the range of 54-55 μm for point A, 56-57 μm for point B and 58-60 μm for point C. It is also noticed that when the spindle is stopped at -6.5 dB (point C), as the pressure is released and intimate contact is gradually lost due to capillary forces, the attenuation is reduced from -6 dB

to values in the -3 to -4 dB range (see right side of Fig. 5). This result is consistent with measured variations in attenuation with variations in pressure between the chuck and the spindle mentioned above.

The presence of the second plateau around -3 dB in Fig. 5 can be explained as the point where the two higher-order modes (LP_{21} and LP_{02}) have a large portion of their power lost to radiation modes. This result also suggests that the lengths of the fibers (2m) are sufficient to provide power evenly distributed among the modes, as one might expect following the model proposed by Gloge.²⁷

In order to determine the precision and repeatability yielded by *in situ* monitoring, 23 fibers were individually lapped with termination of the lapping process aimed at an attenuation level of -6 dB. Various slotted glass holders were used and the spindle was variously dressed or not after each lapping. The histogram and the normal probability plot for attenuation registered at the moment of stopping lapping are depicted in Fig. 6. These graphs show that the monitoring method described above provides an average attenuation of -5.9 dB with a standard deviation of 0.4 dB. The statistical distribution of the data is confirmed to be essentially normal. The histogram and the normal probability plot for the lapped depth h are shown in Fig. 7 where again the distribution is seen to be normal with average lapped depth $h = 58.6 \mu\text{m}$ with standard deviation $0.9 \mu\text{m}$. Elapsed times varying from 12 to 75 minutes were observed in this series of experiments.

In Fig. 8, a photomicrograph (Nomarski contrast) of the cross-section of a single-mode D-fiber fabricated using *in situ* monitoring is shown. For this photomicrograph, white light is launched into the core of the fiber at the distal end. The fiber is cleaved near the center of the 3.0 mm long lapped groove and the cleaved face is polished on $0.5 \mu\text{m}$ diamond polishing paper to remove the spurs and hackle which usually appear after cleaving due to the unusual geometry and lapping-stress patterns contained within the fibers. The fine lineal scores evident on the polished end face are greatly emphasized by use of Nomarski contrast and in fact are less than 60 nm deep as shown by Michelson interferograms (not shown here). In Fig. 8, it is possible to examine the proximity between the core and the flat cladding surface and to observe a well-defined D-shaped cross section. In this case, the lapped depth penetrates about $0.6 \mu\text{m}$ into the $8 \mu\text{m}$ diameter core, nicely within the desired $\pm 1 \mu\text{m}$ precision.

²⁷ D. Gloge, "Optical Power Flow in Multimode Fibers," The Bell Syst Tech. Journal, vol. 51, pp. 1767-1783, 1972.

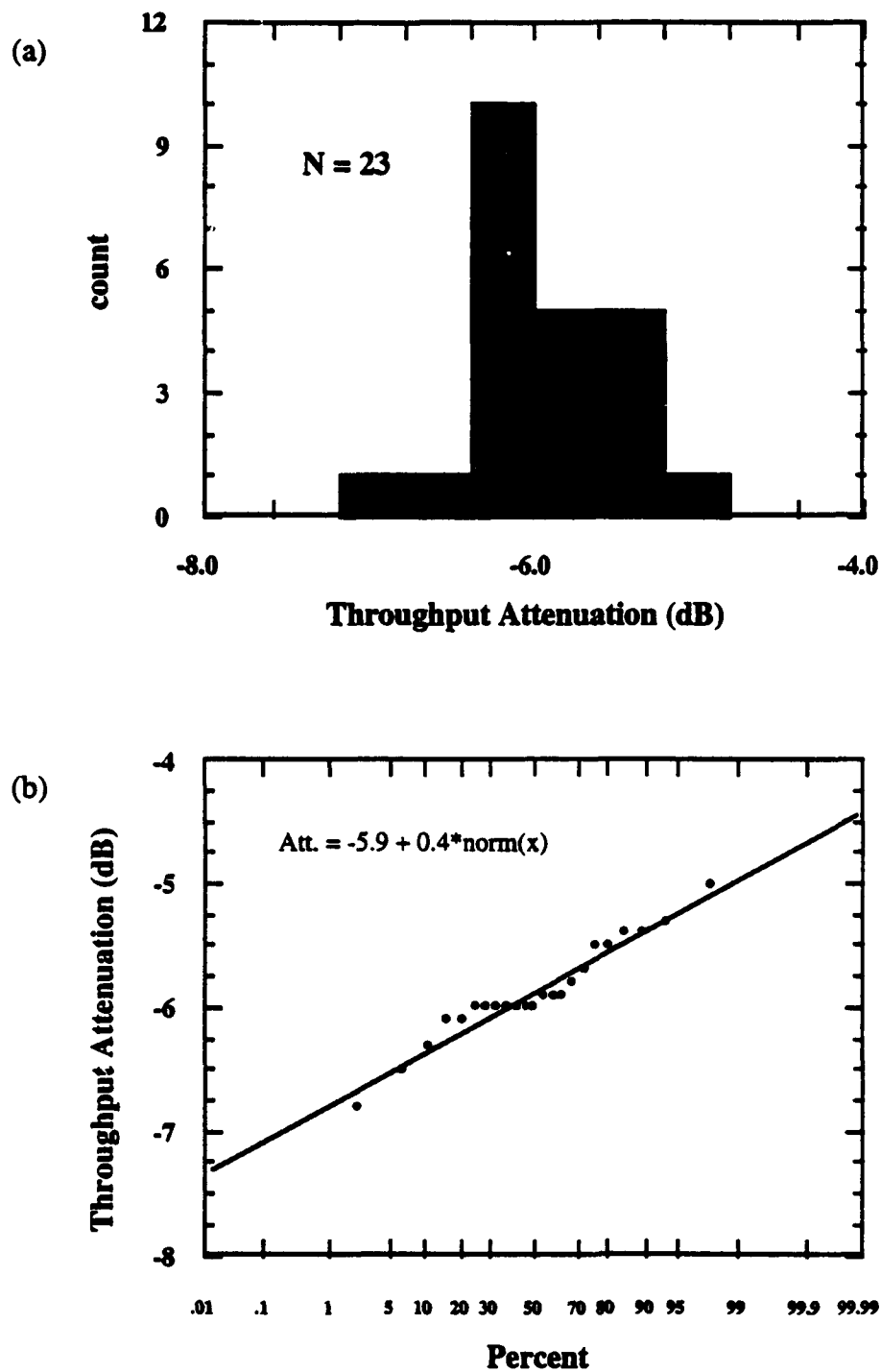


Figure 6. Histogram (a) and normal probability plot (b) for the throughput attenuation (measured just when the lapping is stopped) for 23 fibers lapped using in situ monitoring and a targeted stopping attenuation of -6 dB. The distribution is essentially normal with a mean of -5.9 dB and a standard deviation of 0.4 dB.

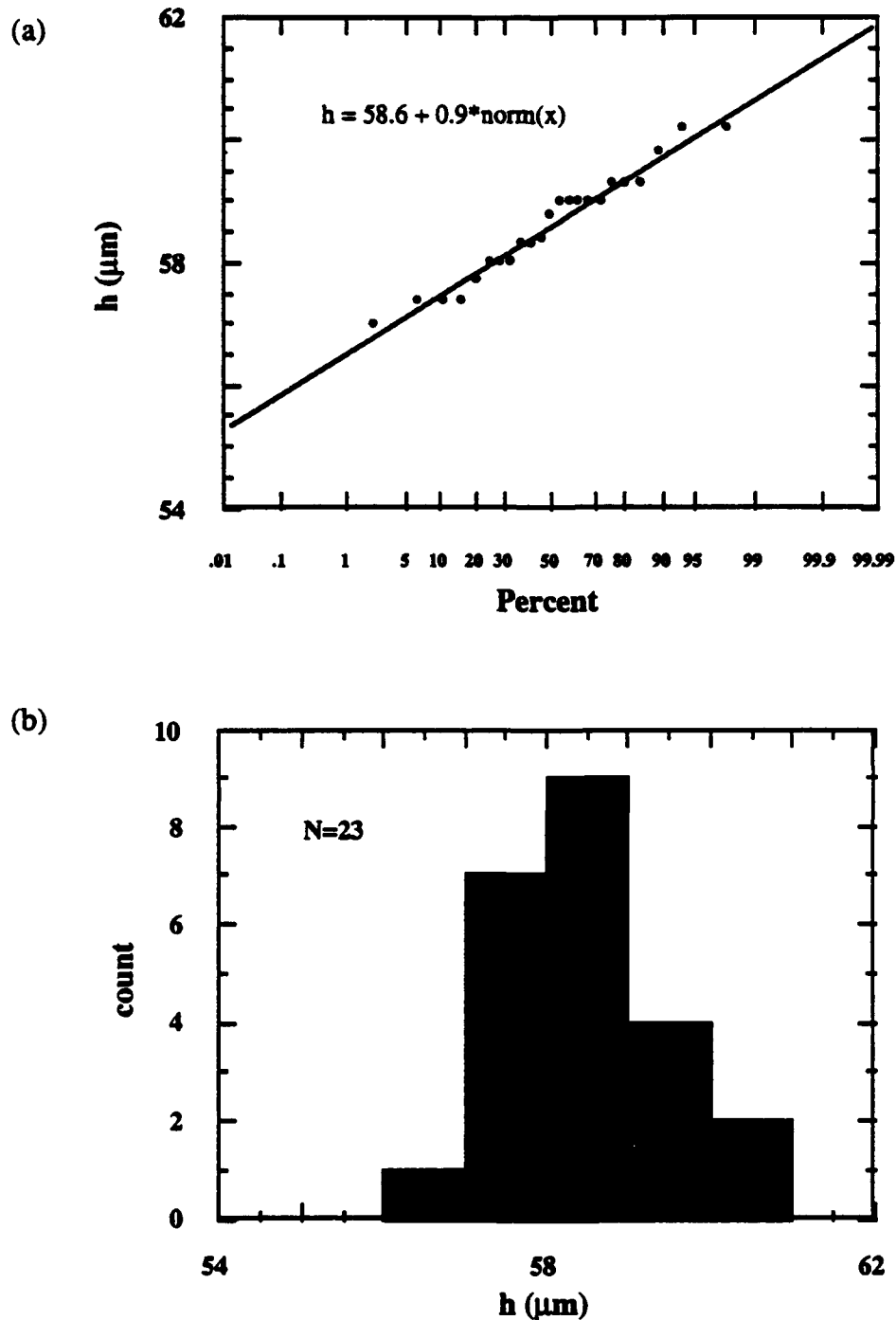


Figure 7. Histogram (a) and normal probability plot (b) for lapped depths for 23 fibers lapped using in situ monitoring and a targeted stopping attenuation of -6 dB. The distribution is very nearly normal with a mean of 58.6 μm and a standard deviation of 0.9 μm .

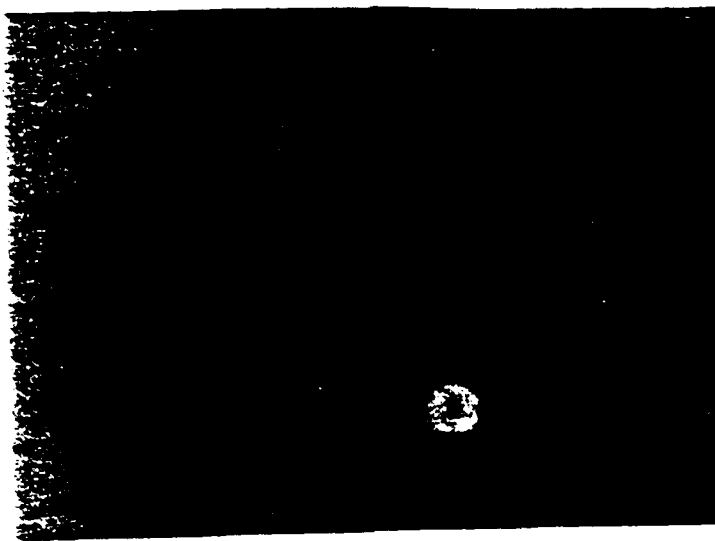


Figure 8. Photomicrograph (Nomarski contrast) of a cross section of a single-mode D-fiber fabricated using mechanical cylinder lapping with *in situ* monitoring to remove 58 μm of cladding layer. White light is launched into the core to show clearly the distance between the core and the flat surface. In this case, the lapped depth penetrates into the core about 0.6 μm .

Conclusion

A technique has been described to locally remove the cladding layer of single-mode optical fibers with one-micron depth precision over a few millimeters of the length of the fiber by use of mechanical lapping with *in situ* optical monitoring. The process relies on the use of a cylinder-lap dressed with diamond to perform high-pressure mechanical lapping. The key new feature of the *in situ* monitoring technique is the recognition that different higher-order propagating modes suffer specific attenuations as the cylinder penetrates into the fiber. The advantages of the technique include relatively rapid overall processing, high lapping rate, good optical surface quality, precision and reproducibility within one micron, no requirement for refractive-index matching fluids, and no sensitivity to ordinary variations in fiber diameter and core eccentricity.

An approximate geometrical-optics analysis was performed to provide qualitative insight. The experimental results are in reasonably good agreement with this analysis, but a fuller electromagnetic mode analysis would be desirable to provide continuous curves of the throughput attenuation as a function of lapped depth. It is important to point out that this kind of monitoring, based upon examination of the higher-order mode structure, provides a possible experimental vehicle to study the modal power distribution in optical fibers.

The overall technique is appropriate for use in the fabrication of single-mode D-fiber which can be used for passive coupling to various planar optical waveguide structures, potentially including such applications as fiber-to-waveguide optical interconnects (both single-fiber connectors and multiple-fiber connector arrays) and fiber-to-electronic device interfaces such as those needed for MESFETs and HEMTs.²⁸

²⁸ R. N. Simons and K. B. Bhasin, "Analysis of Optically Controlled Microwave/Millimeter-Wave Device Structures," IEEE Trans. Microwave Theory Tech., vol. MTT-34, pp. 1349-1355.

Procedure for Making a Planar Star Coupler

Introduction

There are two basic characteristics of this star coupler which contributed to our choice of processing methods:

- single mode operation
- mask patterning using uv-curable acrylic polymers

In order meet the requirement of single mode operation, we designed its constituent waveguides to have a rectangular cross-section measuring $7.5\mu\text{m}$ by $7.5\mu\text{m}$. According to approximate dielectric waveguide mode theory²⁹ a waveguide of these dimensions would require an index of refraction difference (Δn) of about 0.004. We felt that we could successfully tailor the indices of the acrylic polymers with sufficient accuracy to achieve this Δn , and we felt the above waveguide dimensions were achievable with our present photolithographic equipment.

The acrylic resin is a wet, extremely viscous liquid which does not allow contact printing. Further, it is susceptible to an oxygen inhibition reaction during photocuring which inhibits polymerization of the top several microns of the spun-on film³⁰. These characteristics caused our attempts to pattern a single mode coupler using a wide-field ultra-violet lamp exposure to be unsuccessful. As an alternative solution we created a novel procedure which retained the need for a chrome mask while allowing the use of an argon/ion laser instead of our uv lamp.

In this new procedure, an ultraviolet beam from the argon/ion laser is directed down on to a chrome mask beneath which lies the sample to be patterned. The system supporting the mask and sample is mounted on a computer controlled x-y stage. As the stages are moved back and forth in a programmed pattern, the fixed ultraviolet beam scans back and forth across the mask, exposing the sample in the desired areas. The effect is similar to that of spray-painting a pattern through a stencil. The argon/ion laser produces an ultraviolet beam which has a higher degree of collimation and greater power density than the uv lamp. Given these improvements we were repeatedly able to produce waveguides with single-mode dimensions ($4\text{-}10\mu\text{m}$) and excellent resolution ($1\text{-}2\mu\text{m}$).

Preparation of Monomer Mixture

The acrylic monomer mixture used to make our single-mode waveguides is similar to that used in our multimode work³¹. A normal batch would be mixed with these proportions:

²⁹E.A.J. Marcatilli, "Dielectric Rectangular Waveguides and Directional Coupler for Integrated Optics," Bell Syst. Tech. Journal, vol.48, pp. 2071-2102, Sept. 1969.

³⁰Qinrong Yu and Robert Krchnavek, unpublished work.

³¹K. Nakagawa, T. Kowalewski, C.W. Phelps, D.L. Rode, and R.R. Krchnavek, "Optical Channel Waveguides Based on Photopolymerizable Di/Tri Acrylates," in *Optoelectronic Interconnects II*, Ray T. Chen, John A. Neff, Editors, Proc. SPIE 2153, pp. 208-217 (1994).

Table I. Multimode Resin Formulations

Material	Percent by Weight
Resin (Ebecryl 600 or 4883)	69%
Diluent (OTA 480)	30%
Photoinitiator (Irgacure 184)	1%

However, the mixtures used for our single-mode couplers were modified to make the processing easier. First, we increased the proportion of diluent so as to produce a less viscous mixture that could be spun on at lower speeds (≈ 3000 – 4000 rpm) and still result in thicknesses under $10\text{ }\mu\text{m}$. This also served to reduce both the non uniformity in the spun-on film and the edge-bead thickness. Second, we increased the concentration of the photoinitiator in the mixture to reduce the effects of oxygen inhibition.³⁰ The mixture that was settled on for use in the coupler had these proportions:

Table II. Single-Mode Resin Formulations

Material	Percent by Weight
Resin (Ebecryl 600 or 4883)	47%
Diluent (OTA 480)	50%
Photoinitiator (Irgacure 184)	3%

The effect of these changes on the optical and physical characteristics of the acrylic polymers has not yet been established. It is possible that increased diluent concentration has effected adhesion, both to the silicon substrate and to other polymer layers. The physical strength and glass transition temperature may also have changed, and it is certain that the refractive index of the material was altered. Moreover, the waveguide loss of the material may have increased. These questions need to be answered in the future. If it becomes desirable to go back to the original formulation, a possible alternative would be to dissolve methanol or dichloromethane into the resin mixture to decrease viscosity and then add a prebake before curing. Increasing laser power during exposure may remove the necessity for the extra photoinitiator.

Index Tailoring

Our low-index and high-index monomers, when cured with an ultraviolet lamp, have indices of refraction of about 1.494 and 1.549 respectively. It has been shown that these two materials can be mixed to produce indices lying in between those bounds.³¹ In fact for the composition shown in Table I, the index of refraction of a mix of high and low index monomer is linearly proportional to the weight percent of low index in the mixture. Our current experiments indicate that although

the mixture in Table II does not display a similar linear relationship (not yet explained but possibly due to the extra diluent), the results are still quite reproducible. Therefore we are able to tailor cladding and core layer indices of refraction with enough accuracy to achieve $\Delta n = 0.004 \pm 0.001$, required for single-mode operation.

Building the Coupler

The structure of the coupler itself (not including D-fiber linking and packaging) consists of three polymer layers. Each layer represent a distinct step in the processing.

Lower Cladding Layer: First a silicon substrate is prepared which consists of a $\langle 111 \rangle$ oriented 4 in diameter wafer. The wafer is cleaned with solvents and then baked on a hot plate to produce a thin oxide layer. Next an adhesion promoter (3-APS dissolved in de-ionized water) is applied and the wafer is spun dry. Finally the low index monomer (Table I mixture) is spun on at 2500 rpm for 90 seconds to produce a film about 40 microns thick. Note that the cladding material is a Table I mixture while the core will be a Table II mixture. Originally all three layers were to be the same composition, though having different concentrations of high and low-index resin. However it was discovered that the Table II mixture did not adhere well to a cladding layer which was also of Table II composition, and so this change was made.

After the cladding material is spun-on, the wafer is placed in a nitrogen atmosphere and cured under the uv lamp for 2 minutes. Then it is rinsed with acetone and cleaved into desired sample sizes, which is about a 60 mm by 15 mm rectangle for our couplers. Cutting up our wafer after the cladding layer is already in place serve two purposes: it takes less time and is more efficient to produce the cladding layer for several samples at once rather than one at a time, and we can cleave off any edge bead which may disturb the uniform flatness of the surface. Recall that later on in the processing we will have to perform a proximity mask (using the argon-ion laser) and we cannot bring the sample up with in 20 μm if there is a 100 μm thick edge bead in the way.

As has been discussed earlier, curing in nitrogen removes the oxygen inhibition effect and ensures that polymerization will occur all the way to the top of the film. The polymerization reaction is sped up so much in a nitrogen atmosphere that it is actually not possible to achieve good resolution when patterning. This dramatic change in the process characteristics is not clearly understood at this time. However, the cladding layer is a full area exposure and requires no patterning. It is advantageous to cure in nitrogen whenever possible because it produces a much smoother surface than curing in air.

Core Layer: The mask holder built for this procedure consists of a 0.5 in thick, 5 in \times 5 in slab aluminum with a 2 in \times 2 in area cut out of the center, supported by three 6 in posts screwed into the stages. Our 4 in \times 4 in chrome on soda-lime glass mask is held to the underside of the slab with vacuum. A small x-y-z stage slides under the mask to support the sample, and allow the sample to be raised up into the desired proximity with the mask.

The pattern with which the stages move is defined by a Labview 2 computer program which is executed by a Newport PM500 x-y stage controller. Typically we arrange the mask so that the

long axis of the coupler pattern was parallel to the y-axis of the stage, then move the stages back and forth in the x-direction to sweep the laser beam horizontally across the coupler pattern while the y-stage is shifted incrementally. The program used for the coupler delivered was processed with 150 horizontal sweeps of 2.2 cm length, with incremental shifts of 400 μm in the y direction.

Several interdependent factors contribute to the final quality of the waveguides of the coupler being processed:

- laser beam intensity
- laser beam spot size
- scanning velocity
- spacing between scans
- substrate composition
- cladding and core layer thickness
- resin composition

These factors together determine how much energy is delivered to a particular point of the monomer film, which defines how it will polymerize. We found that greater beam intensity and higher scan speed produce better waveguide shape than lower intensity and lower scan speed. Also we believe that a thicker cladding layer and less reflective substrate will require greater beam intensity. If the spacing between scans is too great, the resulting waveguides will develop periodic fluctuations in width along their length. After extensive experimentation we settled on these parameters for our couplers:

Table III. Process Conditions

Laser beam power	19 mW
Scan velocity	17 mm/sec
Scan length	2.2 cm
Number of scans	150
Spacing between scans	400 μm
Substrate	<111> silicon with baked on oxide
Core layer thickness	7.5 μm
Cladding layer thickness	~40 μm

Top Cladding Layer: The 7.5 μm by 7.5 μm waveguides which make up the coupler are not strong enough to survive the transcision sawing procedure that we use to prepare the endfaces of the waveguides. We found that during sawing the waveguides ends would detach from the cladding layer and occasionally be torn off. In addition, after sawing there is a lot of dust (in the form of tiny silicon flakes) resting on the sample. Even the delicate scrubbing procedure required

to clean off these flakes tended to remove sections of the waveguides. Therefore we decided to include a top cladding layer to protect the waveguides during the sawing procedure. This also serves to make the waveguides symmetric.

The top layer is the same material as the lower cladding, but it must be cured in air not in nitrogen. This is because we cannot allow the top layer to cover the guiding ways, and therefore it must be patterned to only cover the waveguides and central region of the coupler. As mentioned above, due to the loss of resolution when curing in nitrogen, any patterning must be done in air. The transicon cut is made with a saw blade which is about 175 μm in width. Therefore if the top cladding layer is patterned so that its edge falls within the 50 μm wide space between the waveguide ends and the ways, then the transicon cut will remove the edge and provide a perfect interface for the D-fiber.

We pattern the upper layer in two steps, using a straight edge on a chrome mask and a lamp exposure. The mask is held with the same system as was described for the preparation of the core layer, except that the system is now mounted on a movable aluminum plate. The upper cladding layer is spun on the coupler, which is placed onto the small x-y-z positioner and slid underneath the mask. Precise positioning of the mask edge just over the spacing between waveguide ends and ways is achieved with the use of a stereo-zoom microscope. Then the entire system is placed under the uv lamp and exposed for 5 minutes. After the first exposure, the sample is turned 180° and the mask edge is positioned over the same space between waveguide and ways on the other side of the coupler. A second 5 minute exposure is then implemented. Finally the sample is removed and rinsed with acetone.

Post-Cure Sample Preparation

Once all three layers of the coupler are in place, the sample is post-baked in a nitrogen ambient. The baking cycle is:

- ramp from 25°C to 125°C over one hour
- hold at 125°C for one hour
- ramp down from 125°C to 25°C over one hour

The post bake is done to help relieve internal stresses in the polymer film and to improve adhesion.

At this time the coupler is transiconed at both ends to provide a flat waveguide interface, and excess silicon is sawed off around the edges of the sample. A small plateau is also cut into the silicon just beyond the ways at both ends of the coupler to provide a surface upon which to glue the D-fibers as well as allowing room for the D-fiber to slide into the ways parallel to the surface. The coupler structure is then mounted with two-part epoxy onto a rectangular silicon submount, measuring 12 cm by 2 cm, to provide support for the coupler and for the packaging.

We begin the process of attaching the D-fiber by simultaneously inserting and aligning two D-fibers, one on each side. This active alignment procedure involves first using visible (632.8 nm) light to verify by eye that both fibers are nearly optimally aligned. Both fibers are held in

positioners which allow x, y, z, θ , and ϕ motion. Given partial alignment, we switch to an infrared input (1300 nm) and optimize power transmitted from fiber to fiber through the coupler. Then while power throughput is still being monitored, we carefully apply a small amount of two-part epoxy just along side each fiber, upon the plateaus created for this purpose. After the epoxy has hardened and it has been verified that each fiber is still in position, both fibers are released from their positioners. Then silicone is applied at two points on each fiber where the buffer has not been stripped off, in order to fix the fibers to the submount and achieve effective strain relief. Additional fibers are then aligned and fixed down until all have been attached.

Final Packaging

As a final step to protect the coupler and its fiber links, two additional measures are taken. First, all exposed fiber (whether buffered or not), from the edge of the submount to the edge of the plateau on both sides, is coated with silicone. Second, a glass plate with a thickness of 0.06" (chosen for its strength and light weight) is cut to be slightly larger than the coupler structure. A silicone bead is drawn around the inside the edge of glass piece, which is then placed over the coupler so that the silicone adheres only to the submount. The glass piece is supported by the silicone bead and does not touch the coupler itself. This simple protective cover provides a water tight seal yet allows the coupler to be easily inspected.

Loss Measurements on the $N \times N$ Star Coupler

Coupler Performance

Once packaging was completed, a final test of the performance of our prototype coupler was conducted. The losses occurring from input to output were measured for each of four possible input-output pairs of the four installed d-fiber. The results are shown in Table IV below. Figure A shows the placement of each d-fiber fitted to the coupler, including a fiber which was over stressed during lapping and broke after installation.

Table IV. Insertion Loss Measurements

Input Fiber	Output Fiber			
	1	2	3	4
1			-28.3 dB	-21.6 dB
2			-24.9 dB	-17.6 dB
3	-28.9 dB	-25.2 dB		
4	-21.9 dB	-18.1 dB		

Let us now look at a breakdown of the losses which we would expect to see occur in the coupler, and compare the result to the data above. First, there will be a loss of 10 dB due to the fact that the power in the input waveguide will be split evenly into ten output waveguides. Second, given that each waveguide has an estimated scattering loss of 1 dB/cm and given that the coupler is about 5 cm in length, we expect 5 dB of scattering losses. Finally, add approximately 1.5 dB coupling loss at each fiber-waveguide interface due to reflection and we have a total expected loss of about 18 dB.

We can see some of the data above compares favorably to this calculation, while some does not. The input/output pair of fibers 2 and 4 appears to have losses equal to or slightly better than expected, whereas the 1 and 3 pair is decidedly worse than expected. There are several loss mechanisms which could be affecting the data, but whose effect has neither been verified or measured. We will list some of these below, along with a brief explanation of each effect:

- Inherent defects in the photomask

The photomask which contains the pattern for our coupler proved to be low quality. Along the input and output waveguides of the pattern there are abrupt jogs and partial gaps, some of which consist of as much as 30% of the width of the waveguide itself. These mask defects will be reproduced and cause scattering losses.

- D-fiber characteristics

The lapped region of a d-fiber rests on the cladding layer of our coupler structure. Since this cladding layer is actually a higher index than the core of the fiber, it is possible that light is coupling through the 1-2 μm of glass left surrounding the fiber core and into the cladding of the coupler. Moreover, although we were able to lap our d-fiber extremely consistently, the lapped depth still had an error of $\pm 1 \mu\text{m}$. This then means that the position of the core with respect to the waveguide must also vary by $\pm 1 \mu\text{m}$, possibly increasing insertion losses.

- Problems with D-Fiber Installation

Difficulties encountered during the attaching of the d-fiber did result in increased insertion loss. The first step in fixing a d-fiber in place requires a drop of epoxy to be placed on the fiber back about 5 mm from the alignment ways. If too much epoxy is applied, capillary forces can cause the epoxy to flow along the fiber and up into the ways. Since the epoxy index of refraction is much higher than the core index, light will most certainly be coupled out of the d-fiber before it can be inserted into the waveguide. This did occur with the first fiber we attached to the coupler, fiber number 3 in Table IV, and partially explains its higher losses. Another difficulty encountered was that during fiber attachment we frequently pressed the face of the fibers up against the waveguide interface. Since we tested many fibers before attaching the final four, several interfaces may have become damaged and dirty.

- Coupler Design

The final possible loss mechanism which we will mention is an obvious one, that the coupler itself may not be operating the way its designers intended it to. Tests of the distribution of light among the ten output waveguides from a single input did suggest a nonuniform split of power. Further, this nonuniform distribution changed shape as a function of input waveguide. We certainly believe that the current coupler design requires characterization using modern numerical computer packages, to see if modifications need to be made.

Conclusion

We have successfully demonstrated that acrylic polymers can be used to fabricate single-mode optical waveguides. The resins that we have formulated are photopolymerizable and therefore provide a simple method of patterning channel waveguides. The photopolymerizable resins do not require plasma or reactive ion etching to remove unwanted material. Instead, a proximity photolithographic technique is used to directly pattern the waveguides using near UV light. Control over the spun-on thickness and the refractive index of the core and cladding resins has been shown. This is essential for fabricating single-mode waveguides with dimensions approximately equal to the core dimensions of optical fiber – a necessary condition to achieve good coupling efficiency between the single-mode optical fiber and the single-mode optical waveguide.

These materials have been used to fabricate a 10×10 optical coupler. Detailed processing steps and the design procedure have been outlined in the report. The coupler was assembled with 4 single-mode optical fibers attached. While fabricating the coupler constitutes a major effort, the usefulness of such a device is highly limited if a suitable means of coupling light into and out of the coupler exists. For this contract, we developed a novel method of coupling single-mode optical fiber to the optical coupler. This required the fabrication of single-mode D fiber. We have successfully lapped single-mode fiber to within $1 \mu\text{m}$ of the core using an *in situ* monitoring technique. The details of the lapping procedure and a theoretical analysis of the *in situ* monitoring technique are detailed in the report. We further developed alignment structures and the transition cut to facilitate higher coupling efficiency with relative ease of fiber-to-waveguide alignment.

The finished coupler performance was measured. The insertion loss was approximately 20 dB with the lowest reading approximately 17.6 dB. When one considers that the splitting of the input signal into 10 signals results in a theoretical minimum insertion loss of 10 dB, the excess loss on the best input/output fiber pairs is 7.6 dB. There are several possible sources for this loss and further research is underway to evaluate the various loss mechanisms.

This work has resulted in several publications:

T.S. Barry, D.L. Rode, M.H. Cordaro, R.R. Krchnavek, and K. Nakagawa, "Efficient Optical Fiber-to-Waveguide Coupling," submitted to the *IEEE Journal of Lightwave Technology*.

M. H. Cordaro, D.L. Rode, T.S. Barry, and R.R. Krchnavek, "Precision Fabrication of D-Shaped Single-Mode Optical Fibers by *in situ* Monitoring," submitted to the *IEEE Journal of Lightwave Technology*.

K. Nakagawa, T. Kowalewski, C.W. Phelps, D.L. Rode and R.R. Krchnavek, "Optical Channel Waveguides Based On Photo-Polymerizable Di/Tri Acrylates," in *Optoelectronic Interconnects II*, Ray T. Chen, John A. Neff, Editors, Proc. SPIE 2153, pp. 208-217 (1994).

T.S. Barry, M.H. Cordara, R.R. Krchnavek, K. Nakagawa, C.W. Phelps, and D.L. Rode, "Efficient Optical Fiber-To-Waveguide Coupling Suitable For Passive Alignment," *IEEE Proc. of the 43rd Electronic Components and Technology Conference*, pp. 1139-1142 (1993).

***MISSION
OF
ROME LABORATORY***

Mission. The mission of Rome Laboratory is to advance the science and technologies of command, control, communications and intelligence and to transition them into systems to meet customer needs. To achieve this, Rome Lab:

- a. Conducts vigorous research, development and test programs in all applicable technologies;
- b. Transitions technology to current and future systems to improve operational capability, readiness, and supportability;
- c. Provides a full range of technical support to Air Force Materiel Command product centers and other Air Force organizations;
- d. Promotes transfer of technology to the private sector;
- e. Maintains leading edge technological expertise in the areas of surveillance, communications, command and control, intelligence, reliability science, electro-magnetic technology, photonics, signal processing, and computational science.

The thrust areas of technical competence include: Surveillance, Communications, Command and Control, Intelligence, Signal Processing, Computer Science and Technology, Electromagnetic Technology, Photonics and Reliability Sciences.